Zhilun Zhang[1], Fengming Hui[1], Mohammed Shokr[1], Mats A. Granskog[1], Bin Cheng[1], Timo Vihma[1], and Xiao Cheng[1]

[1]Affiliation not available

January 10, 2024

Abstract

The neutral form drag coefficient is an important parameter when estimating surface turbulent fluxes over Arctic sea ice. The form drag caused by surface features ($?_{??,??}$) dominates the total drag in the winter, but long-term pan-Arctic records of $?_{??,??}$ are still lacking for Arctic sea ice. In this study, we first developed an improved surface feature detection algorithm and characterized the surface features (including height and spacing) over Arctic sea ice during the late winter of 2009-2019 using the full-scan laser altimeter data obtained in the Operation IceBridge mission. $?_{??,??}$ was then estimated using an existing parameterization scheme. This was followed by applying a satellite-derived backscatter coefficient ($?^{?}_{??}$) to $?_{??,??}$ regression model to extrapolate, for the first time, $?_{??,??}$ to the pan-Arctic scale for the entire winter season over two decades (from 1999 to 2021). We found that the surface features have a larger height and smaller spacing over multi-year ice (1.15 ± 0.21 m and 142 ± 49 m) than over first-year ice (0.90 ± 0.16 m and 241 ± 129 m). The monthly mean $?_{??,??}$ increases through the winter, from 0.2 x 10 -3 in November to 0.4-0.5 x 10 -3 in April. The central Arctic has the largest $?_{??,??}$ (up to 2 x 10 -3), but experienced a drop of ˜50% in the period from 2001/2002 to 2008/2009. The interannual fluctuations in $?_{??,??}$ are strongly linked to the variability of sea ice thickness and deformation, and the latter has become increasingly important for $?_{??,??}$ since 2009.

This article has been accepted for publication in IEEE Transactions on Geoscience and Remote Sensing. This is the author's version which has not been fully edited and content may change prior to final publication. Citation information: DOI 10.1109/TGRS.2023.3347694

Winter Arctic Sea Ice Surface Form Drag During 1999–2021: Satellite Retrieval and Spatiotemporal Variability

Zhilun Zhang, Fengming Hui, Mohammed Shokr, *Senior Member, IEEE*,
Mats A. Granskog, Bin Cheng, Timo Vihma, Xiao Cheng

***Abstract*—The neutral form drag coefficient is an important parameter when estimating surface turbulent fluxes over Arctic sea ice. The form drag caused by surface features ($C_{dn,fr}$) dominates the total drag in the winter, but long-term pan-Arctic records of $C_{dn,fr}$ are still lacking for Arctic sea ice. In this study, we first developed an improved surface feature detection algorithm and characterized the surface features (including height and spacing) over Arctic sea ice during the late winter of 2009–2019 using the full-scan laser altimeter data obtained in the Operation IceBridge mission. $C_{dn,fr}$ was then estimated using an existing parameterization scheme. This was followed by applying a satellite-derived backscatter coefficient (σ_{vv}^{o}) to $C_{dn,fr}$ regression model to extrapolate, for the first time, $C_{dn,fr}$ to the pan-Arctic scale for the entire winter season over two decades (from 1999 to 2021). We found that the surface features have a larger height and smaller spacing over multi-year ice (1.15 ± 0.21 m and 142 ± 49 m) than over first-year ice (0.90 ± 0.16 m and 241 ± 129 m). The monthly mean $C_{dn,fr}$ increases through the winter, from 0.2 × 10^{-3} in November to 0.4–0.5 × 10^{-3} in April. The central Arctic has the largest $C_{dn,fr}$ (up to 2 × 10^{-3}), but experienced a drop of ~50% in the period from 2001/2002 to 2008/2009. The interannual fluctuations in $C_{dn,fr}$ are strongly linked to the variability of sea ice thickness and deformation, and the latter has become increasingly important for $C_{dn,fr}$ since 2009.**

***Index Terms*—Arctic sea ice, turbulent flux, sea ice surface features, form drag coefficient, Operation IceBridge, laser altimeter, scatterometer**

I. Introduction

Rapid changes of Arctic sea ice have been reported by satellite observations since the beginning of the 21st century. These changes are manifested as a great reduction in ice extent, thickness, and multi-year ice (MYI) coverage [1-3], a prolonged melting season [4, 5], and faster ice drift speed [3, 6-8]. These changes have profoundly altered the dynamic and thermodynamic regimes of Arctic sea ice [3, 9, 10], and have significantly contributed to the surface warming in the Arctic [11-13], which has been almost four times faster than that the global mean since the 1980s [14] . This phenomenon is known as the Arctic amplification (AA) [15].

Turbulent fluxes of momentum and heat, modulated by the ice surface topography, are important components of surface fluxes over sea ice. The momentum flux strongly controls the sea ice drift forced by wind [16, 17], while the sensible and latent heat fluxes directly modulate the atmosphere-ice-ocean heat exchange [18, 19]. Increases in the surface turbulent heat fluxes over the Arctic Ocean due to the loss of sea ice have been found to be closely linked to the AA, especially in the winter season [11, 12]. The bulk transfer coefficients for momentum (atmospheric drag coefficient) and sensible/latent heat (scalar transfer coefficients) are at the core of parameterizations of the turbulent fluxes. The drag coefficient determines the momentum exchange between sea ice and the lower atmosphere forced by wind, and is fundamental to deriving scalar transfer coefficients (e.g., Andreas [20], Andreas [21]). With a neutral surface layer stability, the neutral drag coefficient at 10 m reference height (hereafter referred to as the drag coefficient) can be decomposed into contributions from skin drag due to the micro-scale aerodynamic roughness length and form drag caused by the macro-scale surface features, e.g., ridges, snow dunes, and melt ponds [22, 23]. Generally speaking, by assuming a constant skin drag, the form drag can be physically decomposed into the contributions from ridges, snow dunes, ice floe edges, and melt pond edges [24, 25]. In this study, we focused on the form drag from ridges, snow dunes, and other surface features ($C_{dn,fr}$), which dominates the total drag coefficient in winter [26].

** This work was supported by the National Natural Science Foundation of China (41976214). The European Union's Horizon 2020 research and innovation programme provided support to B.C. and T.V. through the Polar Regions in the Earth System project (PolarRES, 101003590), and to M.A.G. through the Climate Relevant interactions and feedbacks: the key role of sea ice and snow in the polar and global climate System project (CRiceS, 101003826). *(Corresponding author: Fengming Hui.)*

Zhilun Zhang, Fengming Hui, and Xiao Cheng are with the School of Geospatial Engineering and Science, Sun Yat-sen University, and Southern Marine Science and Engineering Guangdong Laboratory (Zhuhai), Zhuhai 519082, China, also with the Key Laboratory of Comprehensive Observation of Polar Environment (Sun Yat-sen University), Ministry of Education, Zhuhai 519082, China, and also with the University Corporation for Polar Research, Beijing 100032, China (zhangzhlun@mail2.sysu.edu.cn; huifm@mail.sysu.edu.cn; chengxiao9@mail.sysu.edu.cn).

Mohammed Shokr is with the Science and Technology Branch, Environment and Climate Change Canada, Toronto ON M3H5T4, Canada (mo.shokr.ms@gmail.com).

Mats A. Granskog is with the Norwegian Polar Institute, Fram Centre, Tromsø N-9296, Norway (mats@npolar.no).

Bin Cheng and Timo Vihma are with the Finnish Meteorological Institute, Helsinki 00560, Finland (Bin.Cheng@fmi.fi; Timo.Vihma@fmi.fi).

Airborne and satellite observations have shown great potential in the mapping of Arctic sea ice surface features and $C_{dn,fr}$ at regional and pan-Arctic scales (e.g., Garbrecht, et al. [27], Castellani, et al. [28], Petty, et al. [29], Petty, et al. [30], Duncan and Farrell [31], Mchedlishvili, et al. [32], Ricker, et al. [33]). Petty, et al. [29] (hereafter referred to as P2016) extracted the surface features (defined as features with a minimum height of 0.2 m) over the western Arctic in the late winter of 2009–2014 using the high-resolution Airborne Topographic Mapper (ATM) full-scan elevation data acquired during NASA's Operation IceBridge (OIB) mission. This was the first time that local Arctic sea ice surface features could be mapped from two dimensional (2-D) scanning elevation data, instead of one dimensional (1-D) elevation profiles [27, 28]. Based on P2016, Petty, et al. [30] (hereafter referred to as P2017) investigated the $C_{dn,fr}$ over sections of the Arctic sea ice using ATM data and extrapolated it across the Arctic for the late winter of 2009–2015 using Advanced Scatterometer (ASCAT) data, producing the first map of pan-Arctic $C_{dn,fr}$ to date. Recent studies have shown the potential to map pan-Arctic pressure ridges (and hence $C_{dn,fr}$) from ICESat-2 elevation profiles [31-33], e.g., Mchedlishvili, et al. [32] (hereafter referred to as M2023) derived a new monthly Arctic $C_{dn,fr}$ dataset using ICESat-2 elevation data and revealed the variability of the Arctic sea ice drag coefficient from November 2018 to May 2022.

However, long-term (over a decade) pan-Arctic coverage of $C_{dn,fr}$ is still lacking (e.g., the P2017 algorithm is only suitable for scatterometers in late winter, while M2023 provides this for few recent years). A long-term pan-Arctic $C_{dn,fr}$ could add value to the understanding of basin-scale sea ice characteristics and improve the performance of sea ice models [26, 34]. A long-term record could also reveal response of air-ice interactions to changing Arctic sea ice (e.g., thickness, extent, and deformation) and could help to refine the turbulent flux estimation over the past decades.

This study was aimed at obtaining a long-term wintertime pan-Arctic sea ice $C_{dn,fr}$ and investigating its spatio-temporal variability. Firstly, we improved the P2016 algorithm by applying the Rayleigh criterion and characterized the surface features (including height and spacing) and $C_{dn,fr}$ over Arctic sea ice in the late winter from 2009 to 2019 using OIB ATM data. Secondly, we developed a σ_{vv}^{o}-roughness-$C_{dn,fr}$ regression model (using QuikSCAT and ASCAT data) and performed a 20-year (1999–2021) wintertime daily pan-Arctic $C_{dn,fr}$ extraction by taking the OIB-based $C_{dn,fr}$ and ICESat/ICESat-2 surface topography as references. Finally, we examined the spatial, seasonal, and interannual variability of Arctic sea ice $C_{dn,fr}$ and its relationship to sea ice thickness and deformation.

II. DATA

A. Operation IceBridge

NASA's OIB mission was aimed at measuring various properties of land ice, sea ice, and overlaying snow cover using airborne instruments [35]. The OIB mission was conducted from 2009 to 2019, filling the gap between the Ice, Cloud, and land Elevation Satellite (ICESat) and ICESat-2 missions. In this study, we used the sea ice elevation data obtained from the ATM instrument onboard the OIB aircraft, provided by the National Snow and Ice Data Center (NSIDC) [36, 37]. The ATM instrument is a conically scanning laser altimeter operating at 532 nm, with a nominal swath width of ~250 m and flight altitude of ~460 m [38]. It measures the sea ice surface elevation (relative to WGS84 ellipsoid) with both a footprint and horizontal resolution of ~1–2 m. The OIB sea ice flights were carried out in late winter and early spring (March–April), mainly covering the central Arctic and the region north of Greenland dominated by MYI, and the Beaufort and Chukchi seas (BCS) covered by both MYI and first-year ice (FYI) (Fig. 1). The temporal coverage and the along-track distance of the ATM data in each winter are summarized in Table I. In addition, the position and attitude of the OIB flights, as recorded by the Applanix POS/AV orientation system, were used for the geolocation and segmentation of the ATM data.

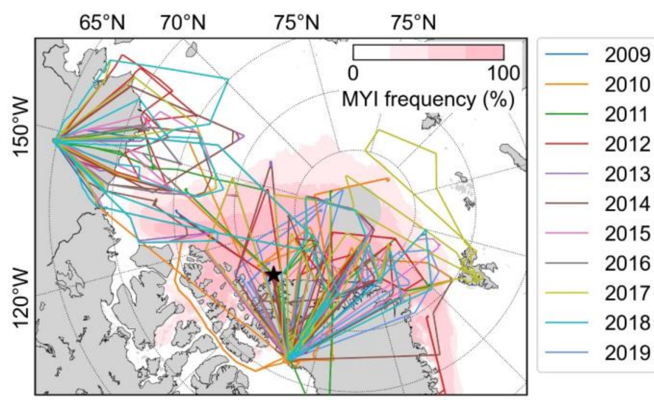

Fig. 1. OIB sea ice flight lines during 2009–2019. The MYI frequency represents the frequency of occurrence of MYI during March and April, 2009–2019, and was calculated using the wintertime daily Arctic sea ice type dataset from Zhang, et al. [39], Zhang, et al. [40]. The hole over 85°N in MYI coverage is due to a lack of data. The black star denotes the location of the example of the 1-km ATM segment shown in Fig. 2a.

TABLE I

TEMPORAL COVERAGE AND ALONG-TRACK DISTANCE OF THE ATM DATA IN EACH YEAR.

Year	Temporal coverage	Number of available days	Along-track distance (km)
2009	March 31–April 25	5	9510
2010	March 23–April 21	8	15398
2011	March 16–April 28	10	13415
2012	March 14–April 10	13	25048
2013	March 20–April 25	10	20138
2014	March 12–April 28	15	26460
2015	March 19–April 3	9	15889
2016	April 20–April 21	2	4038
2017	March 9–April 19	13	23688

This article has been accepted for publication in IEEE Transactions on Geoscience and Remote Sensing. This is the author's version which has not been fully edited and content may change prior to final publication. Citation information: DOI 10.1109/TGRS.2023.3347694

2018	March 22–April 16	8	14711
2019	April 6–April 22	6	7201

B. QuikSCAT and ASCAT

The SeaWinds scatterometer onboard NASA's QuikSCAT satellite (QSCAT) and the Advanced Scatterometer (ASCAT) carried by ESA's MetOp satellites are commonly used radar sensors for large-scale sea ice monitoring, e.g., sea ice extent and type [41, 42], providing an over 20-year record of Arctic sea ice backscatter (1999–2009 for QSCAT and 2006–present for ASCAT). The conically scanning antenna of QSCAT operates in the Ku-band (13.4 GHz) in two polarizations at two fixed angles: HH polarization at 46° and VV polarization at 54.1° [43]. With a swath width of over 1400 m, QSCAT provides daily complete coverage of the Arctic Ocean (excluding the North Pole). ASCAT works in the C-band (5.3 GHz) with two fan-beam antennas on both sides, measuring the backscatter in VV polarization at various incidence angles (25–65°) across the swath [44]. Given that the two scanning swaths at the two sides of the flight path are 550 km wide, separated by a 360-km gap, ASCAT needs one and a half days to cover the entire Arctic region (excluding the North Pole). The surface scattering and volume scattering both contribute to the backscatter of sea ice. The C-band is more sensitive to the surface roughness than the air bubbles inside sea ice (especially MYI), due to the longer wavelength (5.7 cm at 5.3 GHz), compared to the Ku-band (2.3 cm at 13.4 GHz) [45, 46]. In this study, we used the daily gridded Arctic sea ice backscatter in VV polarization (σ_{vv}^{o}) from QSCAT and ASCAT during the winter (November–April) of 2002–2021, provided by the French Research Institute for Exploitation of the Sea (IFREMER), with a spatial resolution of 12.5 km. The ASCAT σ_{vv}^{o} was normalized to the incidence angle of 40°.

C. ICESat and ICESat-2 sea ice surface height

One of the objectives of the ICESat (2003–2009) and ICESat-2 (2018–present) missions was to measure the elevation changes of the ice sheet and sea ice in polar regions. The Geoscience Laser Altimeter System (GLAS) deployed on ICESat, working in the 1064-nm channel, provides surface elevations with footprints of ~70 m and intervals of 170 m [47]. Each ICESat measurement campaign lasted for one month (mainly conducted in February–March, May–June, and October–November) with a 91-day exact repeat and a 33-day sub-cycle in the Arctic [48]. The Advanced Topographic Laser Altimeter System (ATLAS) carried by ICESat-2, operating at 1064 nm, has six beams arranged in three pairs [49]. The transmitted laser pulses for each beam are spaced at 0.7-m intervals, while the sea ice height is derived from each 150-photon segment, corresponding to a horizontal resolution of ~60–150 m, depending on the surface type [50]. ICESat-2 operates in a 91-day exact repeat with sub-cycles of 4 and 29 days over the Arctic Ocean. In this study, we used the GLAS/ICESat L2 Sea Ice Altimetry data [51] and the ATLAS/ICESat-2 L3A Sea Ice Height data [50], provided by NSIDC, to calculate the Arctic sea ice surface roughness in a 12.5-km window. The sea ice elevation/height data were selected for the winter months (November to the following April) during 2003–2009 and 2018–2020. All of the ICESat data were used, and the data on the 5th, 15th, and 25th of each month were selected for the ICESat-2 period.

D. Sea ice concentration and type

The sea ice concentration data were used to identify the ice cover with a concentration larger than 90%. All estimates of the surface features and $C_{dn,fr}$ were conducted for this range of concentration (very close pack ice between 90% and 100%, and compact ice of 100% concentration). We selected two products of passive microwave sea ice concentration. Before 2002, the 25-km daily sea ice concentration from SSM/I and SSMI/S based on the NASA Team (NT) [52] algorithm was used. From 2002, we used the AMSR-E/AMSR2 daily sea ice concentration based on the Arctic Radiation and Turbulence Interaction Study (ARTIST) Sea Ice (ASI) algorithm [53], with a higher spatial resolution of 6.25 km. The gap between AMSR-E and AMSR2 was filled by the SSMIS sea ice concentration using the same ASI algorithm. The error of these products is less than 10% in winter [53, 54]. The NT-based and ASI-based sea ice concentration data were obtained from the NSIDC and the University of Bremen, respectively. The wintertime daily Arctic sea ice type data were acquired from Zhang, et al. [39], in which the resolution-enhanced (4.45 km) scatterometer and radiometer data were used to distinguish MYI from FYI based on an adaptive machine learning classification algorithm. This dataset covers the winter of 2002–2017 and has been extended to 2020 [40]. Validation against synthetic aperture radar (SAR) interpretation has shown an overall classification accuracy of over 90% [39]. The sea ice concentration and sea ice type products were resampled onto the same 12.5-km grid as the scatterometer data.

E. Sea ice deformation and thickness

The NSIDC Polar Pathfinder Daily EASE-Grid Sea Ice Motion (Version 4) product [55] was selected to calculate the sea ice divergence and convergence as the deformation metric. The spatial resolution of the ice motion product is 25 km, with a bias of less than 2 km d^{-1} against buoys [56]. It should be noted that the ice motion vector is unavailable in the Canadian Archipelago due to the narrow sea water passages. The daily Arctic sea ice thickness was obtained from the pan-Arctic Ice Ocean Modeling and Assimilation System (PIOMAS) Arctic Sea Ice Volume Reanalysis [57]. The uncertainty of the PIOMAS sea ice thickness is less than ±0.8 m, and this product has been shown to be reliable in rebuilding the long-term record of Arctic sea ice volume [58, 59]. The mean spatial resolution of the PIOMAS sea ice thickness is approximately 22 km. Both the sea ice motion and thickness data cover the winter of 1999–2021, and were resampled onto the same 12.5-km grid as the scatterometer data.

III. Methods

A. Characterizing surface features using OIB ATM data

A surface feature is defined here as a surface obstacle with an elevation that exceeds 20 cm above the leveled ice surface. Surface features include ridges, snow dunes, and hummocks, but the type of feature was not identified in this study. The 20-cm threshold has been shown to be appropriate to detect both

This article has been accepted for publication in IEEE Transactions on Geoscience and Remote Sensing. This is the author's version which has not been fully edited and content may change prior to final publication. Citation information: DOI 10.1109/TGRS.2023.3347694

thick (e.g., pressure ridges) and small features (e.g., snow dunes) [29, 30]. However, a threshold of 60 or 80 cm is sometimes used to detect large features [28, 33]. Basically, we followed the method of surface feature detection established in Petty, et al. [29], but with a few changes and updates (described below). The overall procedure is summarized below, with an example shown in Fig 2.

1) Preprocessing of the ATM data: The OIB ATM data were separated into 1-km segments over sea ice using the accurate position information from the POS/AV data. To ensure reasonable data coverage and reliable feature identification, we discarded the 1-km ATM segments with a poor quality, i.e., mean pitch or roll larger than 5°, mean altitude out of the range of 300–700 m, and the number of points less than 75% of the annul mean (threshold of 15000 for 2009–2016 and 45000 from 2017). An example of the raw ATM data in 1-km segments is shown in Fig. 2a. Pressure ridges can be found in the middle and lower parts of the image, and leads exist in the lower right.

2) Cumulative distribution of the elevation data: This was calculated for each 1-km ATM segment (an example is shown in Fig. 2b). We used a frequency window (width of 0.2) to search the elevation range with the smallest increase of elevation. The elevation corresponding to the median of the frequency range (the blue color in Fig. 2b) was then defined as the level ice elevation (the dashed line in Fig. 2b). For the example of the 1-km segment (Fig. 2a), the level ice elevation with respect to the WGS84 ellipsoid is 9.7 m, with the smallest elevation increase in the frequency range of 0.29–0.49.

3) Gridded ATM points: For all the ATM points in each 1-km segment, the surface height was calculated by subtracting the raw elevation from the level ice elevation. The ATM points were then projected and interpolated onto a polar stereographic grid with a spatial resolution of 2 m (Fig. 2c). The 2-m resolution is reasonable because the mean spacing of the ATM points is less than 2 m. The bilinear interpolation method was used rather than the linear scheme used in P2016, which is one of the updates of the proposed method. We supposed that the bilinear-interpolated topography would be more realistic since the ATM points from the four surrounding orthogonal directions are involved in the interpolation for each grid cell. The results show that the surface feature height derived using the bilinearly interpolated data is 0.14 m (9%) smaller than that obtained using linear interpolation (Fig. S1).

4) Identifying individual features: For each 1-km segment, areas with a surface height below 20 cm were masked (the blank regions in Fig. 2c). The retained parts were then segmented into several unconnected components. The components with an area less than 100 m^2 were discarded. For each component, we searched all the local maxima with a distance between each other larger than 10 m. This value has been commonly used in surface feature separation, e.g., Martin [60] and Castellani, et al. [28]. The square markers in Fig. 2e and Fig. 2f denote the local maxima of the 1-km segment shown in Fig. 2c. However, not all the local maxima were retained because some may come from the same surface feature, e.g., the pressure ridges with consecutive local maxima (the east–west ridge shown in Fig. 2e). To avoid over-segmentation caused by these maxima, the Rayleigh criterion, which has been widely used in surface feature identification based on linear profile data [28, 31, 60], was applied to the full-scan ATM data. This is the major improvement to the P2016 algorithm, in which the Rayleigh criterion was not applied. Specifically, we retained the local maxima with a height more than twice as large as the height of the surrounding troughs (the pink squares in Fig. 2e and Fig. 2f). A more detailed analysis of the effect of the Rayleigh criterion is provided in Section V-A. Finally, the watershed algorithm [61] was used to separate the retained local maxima and find the boundary separating each feature (Fig. 2e and Fig. 2f). The watershed algorithm took the local maxima as seeds and simulated a flooding process. Basins formed around each seed as the "water" level rose. When two basins met, they were separated by a watershed line. Once the flooding process was complete, the regions enclosed by the watershed lines represented the segmented surface features. For the given ATM example, a total of 114 surface features were identified (Fig. 2d).

This article has been accepted for publication in IEEE Transactions on Geoscience and Remote Sensing. This is the author's version which has not been fully edited and content may change prior to final publication. Citation information: DOI 10.1109/TGRS.2023.3347694

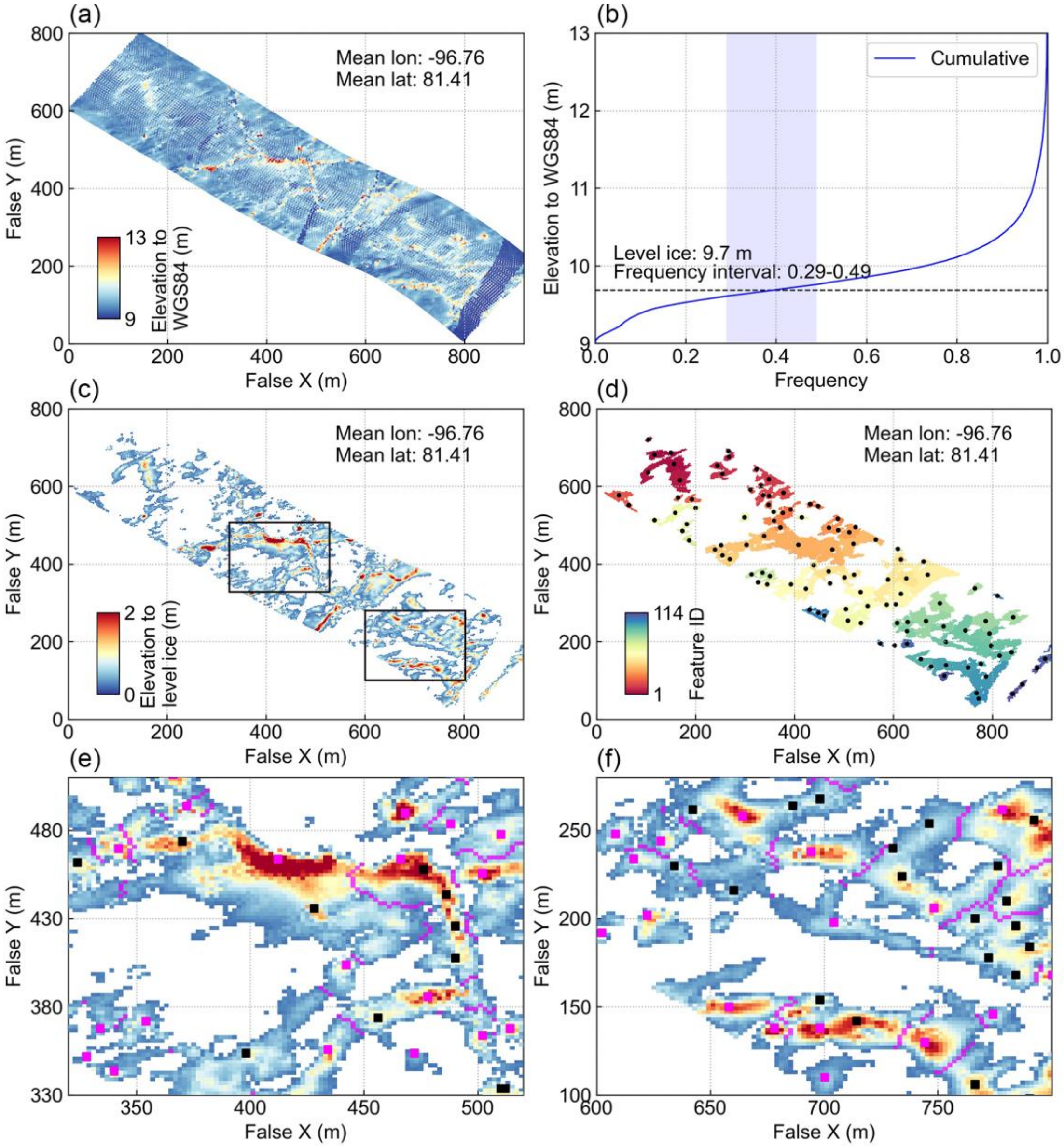

Fig. 2. Example showing the surface feature detection method for a 1-km segment of OIB ATM data from March 16, 2011. The location of the 1-km segment is marked as the black star in Fig. 1. (a) Surface elevation from the ATM data. (b) Cumulative distribution of the raw elevation data. (c) Gridded elevation (larger than 0.2 m relative to level ice). (d) Identified surface features and their centroids (black points). (e)–(f) Enlarged views of the relative elevation (the frame in Fig. 2c) with local maxima (square points). The pink squares represent the local maxima preserved after applying the Rayleigh criterion. The boundaries between adjacent features are shown by the pink lines. “False X (Y)” in (a) and (c-f) is the x- (y-) coordinate value relative to the southwest corner of the bounding box of the 1-km ATM segment.

B. Calculating surface feature height, spacing, and form drag coefficient

Surface feature height h_f and spacing D_s are two key parameters when characterizing surface feature distributions and parameterizing $C_{dn,fr}$. In this study, we followed P2016, P2017, and M2023 to calculate h_f, D_s, and $C_{dn,fr}$ based on OIB ATM data. It should be noted that the h_f, D_s, and $C_{dn,fr}$ were calculated as 10-km means (from 10 consecutive 1-km segments). The length of 10 km is considered to be an appropriate length scale, which fits the climate model and microwave satellite observations. For each 10-km segment, we assigned the central point of the segment to represent the mean h_f, D_s, and $C_{dn,fr}$. The detailed parameterizations of h_f, D_s, and $C_{dn,fr}$ are given below.

h_f is defined as the maximum height of each individual surface feature. The mean h_f is the average from all the surface features within a 10-km segment, based on the assumption of random feature orientation. The mean D_s represents an average spacing of the surface features within a given segment (length of 10 km) and can be calculated as [62]:

$$D_s = \frac{\pi}{2F_d} \quad (1)$$

where F_d is the feature density (number of features per meter) in the 10-km segment, defined as [22, 63]:

$$F_d = \sum_{i=1}^{N} \frac{L_f^i}{S_A} \tag{2}$$

where N is the count of all the surface features, S_A is the total ice area of the segment (equal to the number of pixels of the gridded ATM elevation in the 10-km segment multiplied by the area of the pixel (4 m^2)), and L_f is the length of each individual feature within the 10-km segment. By simplifying the shape of each feature as an ellipse, L_f can be defined as [29]:

$$L_f = \frac{2}{\sqrt{\pi}}\sqrt{S_f R} \tag{3}$$

$$R = \sqrt{C_p / C_s} \tag{4}$$

where S_f and R are the area and the degree of elongation of each surface feature, respectively. S_f is equal to the number of pixels of the feature multiplied by the area of the pixel (4 m^2). R can be calculated using the primary and secondary eigenvalues (C_p and C_s, respectively) of the feature covariance matrix [30]. The $C_{dn,fr}$ over compact sea ice can be described as follow [27]:

$$C_{dn,fr} = \frac{c_w}{\pi}\frac{h_f}{D_s}\frac{\left[\ln\left(h_f/z_0\right) - 1\right]^2 + 1}{\ln\left(h_{ref}/z_0\right)} \tag{5}$$

where h_f and D_s are the 10-km mean surface feature height and spacing, respectively, c_w is the coefficient of resistance of a single feature related to the surface feature height ($c_w = 0.15h_f + 0.19$) [27], z_0 is the surface roughness length of level sea ice (1×10^{-5} m), and h_{ref} is the reference height of wind above the ice surface (here 10 m).

C. Estimating the pan-Arctic surface form drag coefficient from satellite microwave observations

We used the backscatter coefficient in VV-polarization (σ_{vv}^o) obtained from QSCAT and ASCAT to extrapolate the OIB-based $C_{dn,fr}$ (acquired in March and April) to the pan-Arctic scale during the winter months (November to the following April) for 1999–2021. A simple empirical regression model was developed. To extrapolate the OIB-based $C_{dn,fr}$ to the entire winter period, σ_{vv}^o should depict the trend and variability in surface roughness (relevant to $C_{dn,fr}$). Following Kwok, et al. [47], Farrell, et al. [49], we derived the sea ice surface roughness (σ_h, defined as the standard deviation of the surface height in a 12.5-km window) from ICESat (2003–2009) and ICESat-2 (2018–2020) and linked it with the σ_{vv}^o from QSCAT and ASCAT. A new σ_{vv}^o - σ_h - $C_{dn,fr}$ regression model was then developed to estimate the wintertime $C_{dn,fr}$ using data from scatterometers. As mentioned before, the retrieval was conducted for regions with a sea ice concentration over 90%, avoiding the effect of ice floe edges on the $C_{dn,fr}$ estimation (present mainly in the marginal ice zone). The steps were as follows:

1) Establishment of the monthly regression between σ_{vv}^o and σ_h. Given that ICESat/ICESat-2 needs about one month for an entire coverage of the Arctic Ocean, a monthly regression between σ_{vv}^o from QSCAT/ASCAT and σ_h from ICESat/ICESat-2 was established, using an exponential function $y = Ae^{Bx}$ (where A and B are constants) (Fig. 3). The regression shows good correlation, with the correlation coefficient $R > 0.65$ and low mean bias (MB) and standard deviation (STD) for both the QSCAT (Fig. 3a–f) and ASCAT (Fig. 3g–l) periods. It should be noted that ICESat mainly worked in October–November and February–March according to the annual campaign [64], so the ICESat data are mostly unavailable for December, January, and April (Table II). Thus, statistical regression for these months was not considered.

TABLE II

NUMBER OF PAIRS FOR LINKING σ_{vv}^o FROM QSCAT/ASCAT AND σ_h FROM ICESAT/ICESAT-2.

Comparison	Winter	Nov	Dec	Jan	Feb	**Mar**	**Apr**
QSCAT vs. ICESat	2003/2004	14533	-	-	23785	37202	-
	2004/2005	10241	-	-	17255	45822	-
	2005/2006	26799	-	-	9033	54478	-
	2006/2007	20522	-	-	-	31517	16555
	2007/2008	4143	-	-	24533	37108	-
	2008/2009	2924	20298	-	-	37480	16425
	All	**79162**	**20298**	-	**74606**	**243607**	**32980**
ASCAT vs. ICESat-2	2018/2019	5197	4521	6326	5406	5765	4334
	2019/2020	3125	4903	6851	6257	6101	4527
	All	**8322**	**9424**	**13177**	**11663**	**11866**	**8861**

This article has been accepted for publication in IEEE Transactions on Geoscience and Remote Sensing. This is the author's version which has not been fully edited and content may change prior to final publication. Citation information: DOI 10.1109/TGRS.2023.3347694

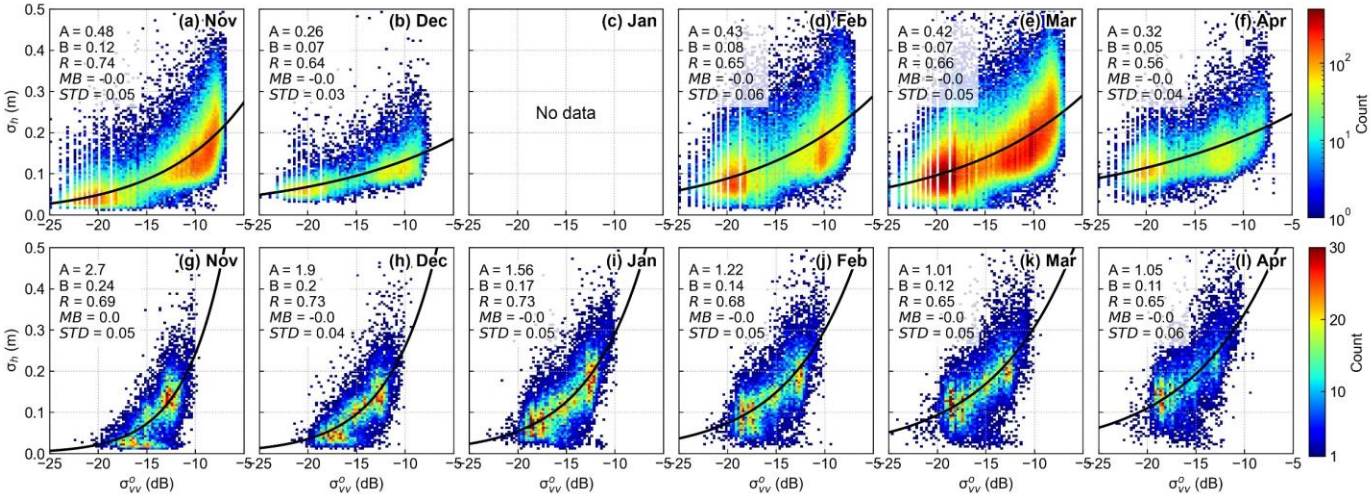

Fig. 3. Scatter plots of σ_{vv}^o from QSCAT/ASCAT and σ_h from ICESat/ICESat-2 for the winter months. (a)–(f) QSCAT vs. ICESat during 2003/2004–2008/2009. (g)–(h) ASCAT vs. ICESat-2 during 2018/2019–2019/2020. The curves represent the function $y = Ae^{Bx}$.

2) Calculation of the daily regression coefficients and daily $\boldsymbol{\sigma_h}$. Fig. 4 shows the variability of the monthly regression coefficients *A* and *B* for QSCAT and ASCAT. Both coefficients decrease throughout the winter, especially for ASCAT. Assuming that the monthly regression coefficients represent the daily coefficients on the 15th of each month, a B-spline function [65] was used to fit the correlation between the days of winter (1–181, from November 1 to April 30) and the daily coefficients. B-spline function is a statistical modeling technique that uses piecewise-defined polynomial functions for regression between a dependent variable and one or more independent variables. The knots in B-spline function determine the boundaries of the segments, the coefficients determine the shape and height of the polynomial within each segment, and the degree determines smoothness and flexibility of the curve. The highest degree of the spline fit was set to be 1 and 3 for QSCAT and ASCAT, respectively. QSCAT coefficients for December and April were not included in the fit, due to the small amount of data, as mentioned before. The B-spline function was finally fitted once the squared differences between the observed variable and predicted variable (the coefficient A or B) is minimized. The details of the fit and the daily coefficients are summarized in Table III and Tables S1 and S2, respectively. The daily coefficients were then used to estimate the daily σ_h from QSCAT (1999–2009) and ASCAT (2006–2021), respectively.

TABLE III
DETAILS OF THE B-SPLINE FUNCTIONS USED TO ESTIMATE THE DAILY REGRESSION COEFFICIENTS A AND B.

Sensor	Regression coefficient	Vector of knots	B-spline coefficients	Degree
QSCAT	*A*	[15, 15, 136, 136]	[0.483, 0.413, 0, 0]	1
	B	[15, 15, 136, 136]	[0.115. 0.071, 0, 0]	1
ASCAT	*A*	[15, 15, 15, 15, 166, 166, 166, 166]	[2.678, 1.340, 0.993, 1.029, 0, 0, 0, 0]	3
	B	[15, 15, 15, 15, 166, 166, 166, 166]	[0.241, 0.174, 0.116, 0.112, 0, 0, 0, 0]	3

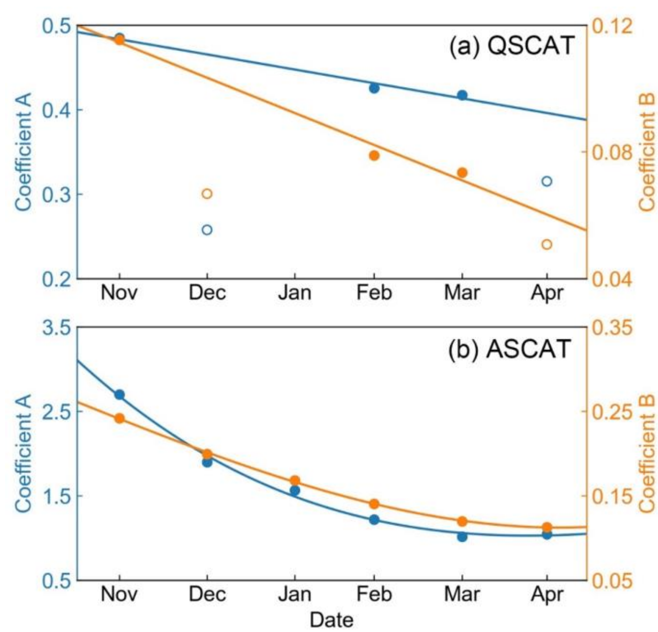

Fig. 4. Monthly coefficients for (a) QSCAT and (b) ASCAT using the function $y = Ae^{Bx}$ when regressed against σ_h from ICESat/ICESat-2. The curves indicate the daily coefficients obtained using the B-spline fit. The degree of fit is 1 and 3 for QSCAT and ASCAT, respectively. The solid (hollow) points indicate the monthly coefficients used (not used) in the B-spline fit.

This article has been accepted for publication in IEEE Transactions on Geoscience and Remote Sensing. This is the author's version which has not been fully edited and content may change prior to final publication. Citation information: DOI 10.1109/TGRS.2023.3347694

3) Estimation of daily wintertime $C_{dn,fr}$ based on OIB observations. Fig. 5 shows the distribution of the scatterometer-based σ_h and the OIB-based $C_{dn,fr}$ from all the years. The scatterometer-based σ_h was obtained from the previous regression of the daily data between σ_{vv}^o and the ICESat/ICESat-2 σ_h. The exponential function $y = Ae^{Bx}$ (A and B are constants) has a similar fit to the polynomial functions but with a smaller number of constants, and was selected for the regression. The regression function using the OIB-based $C_{dn,fr}$ from all the years shows a high R (>0.74) and small bias for both the QSCAT and ASCAT periods. The overall regression using the data from all the years also performs similarly to the regressions using data from each single year (not shown). Hence, we used the overall regression coefficients to estimate the wintertime $C_{dn,fr}$ for the QSCAT period and ASCAT period. Coefficient A is 0.05 (0.09) and coefficient B is 13.29 (7.96) for the QSCAT (ASCAT) period.

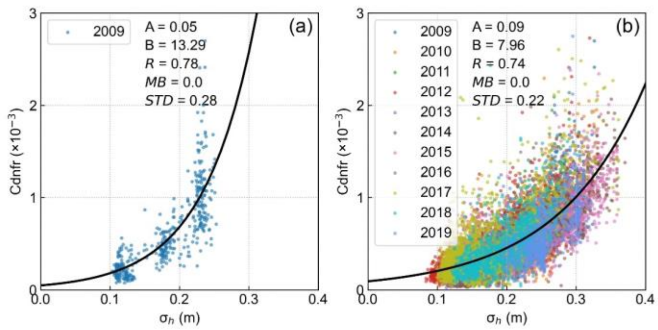

Fig. 5. Scatter plots of the scatterometer-based σ_h vs. OIB-based $C_{dn,fr}$ for all the years. (a) QSCAT. (b) ASCAT. The curves indicate the function $y = Ae^{Bx}$.

IV. Results

A. Distribution of the OIB-based surface features

The frequency distributions of the 10-km mean h_f, D_s, and $C_{dn,fr}$ over the Arctic Ocean and the surrounding seas are shown in Fig. 6, and the maps and statistics for these parameters are given in Fig. 7 and Table IV, respectively. For the frequency distribution (Fig. 6a–c), h_f ranges from 0.5 to 2 m during March and April, with an average (± standard deviation) of 1.07 ± 0.22 m. A long tail is observed for D_s, ranging from 60 to 600 m, with an average of 171 ± 94 m. The $C_{dn,fr}$ mainly ranges within 0–1.5 × 10^{-3}, with a tail of up to 2.5 × 10^{-3} and an average of 0.53 ± 0.34 × 10^{-3}. We used three common functions (i.e., normal, log-normal, and exponential functions) to examine the probability distributions of h_f, D_s, and $C_{dn,fr}$ (Fig. 6d–f). The Chi-square (χ^2) test [66] was used to test the degree of fit (the lower the χ^2, the better the fit). Both h_f and $C_{dn,fr}$ follow log-normal distributions. Although none of the three functions fit the distribution of D_s, the tail (D_s > 200 m) is closer to an exponential distribution.

The spatial distributions of the 10-km mean h_f, D_s, and $C_{dn,fr}$ in the late winter of 2010/2013/2016/2019 are illustrated in Fig. 7, overlaid on the map of MYI coverage. Maps of h_f, D_s, and $C_{dn,fr}$ for each year are given in Figure S2, S3, and S4 respectively. Generally speaking, the Arctic Basin and the Canadian Arctic (dominated by MYI) show larger h_f and $C_{dn,fr}$ and smaller D_s than the surrounding areas (dominated by FYI). The average h_f, D_s, and $C_{dn,fr}$ for MYI are 1.15 m, 142 m, and 0.64 × 10^{-3}, respectively (Table IV). For FYI, the values are 0.90 m, 241 m, and 0.29 × 10^{-3}, respectively (Table IV). This indicates stronger surface deformation over MYI than over FYI, along with more and higher surface features, i.e., ridges, snow dunes, and hummocks. In addition, the closer to the coastline of Greenland and the Canadian Arctic Archipelago (CAA), the more severe the deformation of sea ice is, resulting in larger $C_{dn,fr}$.

Table IV lists the annual means of h_f, D_s, and $C_{dn,fr}$ over all ice, MYI, and FYI covered by OIB flights. In general, no significant trend can be observed for h_f, D_s, or $C_{dn,fr}$ during the late winter of 2009–2019. Since the ice area covered by the OIB sea ice flight differs from year to year due to different missions (as shown in Fig. 1, Figure S2–S4, and Table S3), it is difficult to fully account for the interannual variability of h_f, D_s, or $C_{dn,fr}$. For instance, the low value of h_f and $C_{dn,fr}$ in 2016 (0.99 m and 0.38 × 10^{-3}, respectively) results from the lack of data in the area dominated by MYI (Fig. 7). Nevertheless, the minimum of h_f and $C_{dn,fr}$ in 2013 (0.97 m and 0.38 × 10^{-3}, respectively) is probably due to the loss of large surface features caused by the coincident loss of MYI coverage, with the minimum extent less than 2 × 10^6 km^2, as shown in Zhang, et al. [39].

This article has been accepted for publication in IEEE Transactions on Geoscience and Remote Sensing. This is the author's version which has not been fully edited and content may change prior to final publication. Citation information: DOI 10.1109/TGRS.2023.3347694

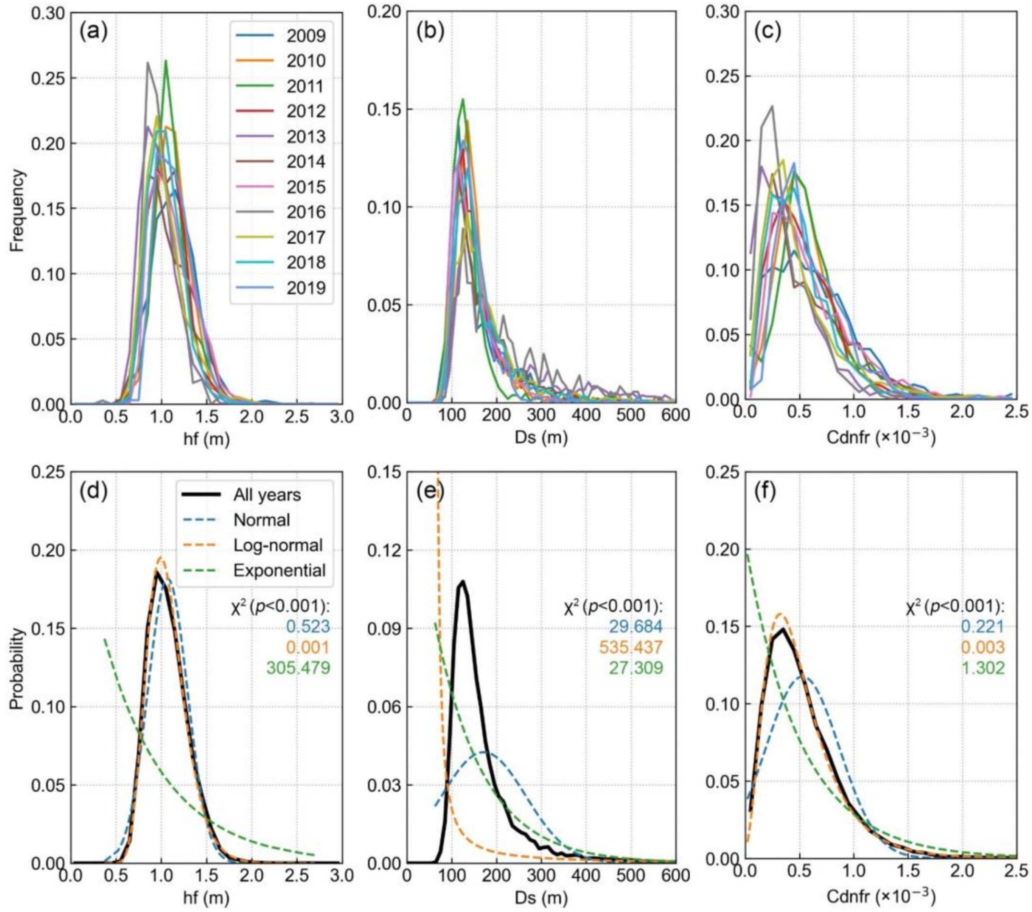

Fig. 6. (a)–(c) Frequency distributions of the OIB-based 10-km mean h_f, D_s, and $C_{dn,fr}$ for late winter (March and April) in 2009–2019. (d)–(f) Same but from all years and their probability distributions using normal, log-normal, and exponential fits.

TABLE IV

ANNUAL MEAN h_f, D_s, AND $C_{dn,fr}$ AND THEIR STANDARD DEVIATIONS FOR THE 10-KM SEGMENT FOR TOTAL ICE COVER, MYI, AND FYI, RESPECTIVELY. THE DATA WERE OBTAINED DURING OVERPASSES OF OIB-ATM.

Year	h_f (m)			D_s (m)			$C_{dn,fr}$ ($\times10^{-3}$)		
	Total	MYI	FYI	Total	MYI	FYI	Total	MYI	FYI
2009	1.15±0.24	1.21±0.21	0.87±0.11	155±69	135±48	246±80	0.65±0.41	0.74±0.39	0.23±0.11
2010	1.12±0.19	1.17±0.19	0.89±0.18	156±67	145±52	244±144	0.57±0.30	0.63±0.32	0.31±0.24
2011	1.10±0.19	1.15±0.19	0.89±0.12	155±110	130±42	398±316	0.60±0.32	0.68±0.32	0.25±0.17
2012	1.07±0.20	1.14±0.18	0.95±0.19	158±60	133±28	205±75	0.54±0.33	0.64±0.31	0.36±0.30
2013	0.97±0.20	1.06±0.17	0.81±0.11	228±150	153±44	360±173	0.38±0.26	0.50±0.23	0.16±0.11
2014	1.08±0.24	1.15±0.24	0.86±0.12	177±99	155±68	249±137	0.53±0.36	0.62±0.36	0.25±0.14
2015	1.12±0.23	1.19±0.23	0.95±0.14	149±55	137±51	177±51	0.61±0.37	0.71±0.38	0.36±0.18
2016	0.99±0.18	1.13±0.15	0.93±0.15	226±127	134±38	264±132	0.38±0.27	0.62±0.25	0.28±0.20
2017	1.04±0.23	1.17±0.23	0.90±0.15	174±86	137±42	219±106	0.50±0.37	0.69±0.40	0.31±0.20
2018	1.04±0.18	1.12±0.16	0.93±0.16	165±75	135±41	212±91	0.49±0.28	0.61±0.26	0.32±0.22
2019	1.14±0.19	1.14±0.19	1.01±0.26	149±54	146±45	309±173	0.60±0.30	0.60±0.30	0.38±0.38
All	**1.07±0.22**	**1.15±0.21**	**0.90±0.16**	**171±94**	**142±49**	**241±129**	**0.53±0.34**	**0.64±0.34**	**0.29±0.22**

This article has been accepted for publication in IEEE Transactions on Geoscience and Remote Sensing. This is the author's version which has not been fully edited and content may change prior to final publication. Citation information: DOI 10.1109/TGRS.2023.3347694

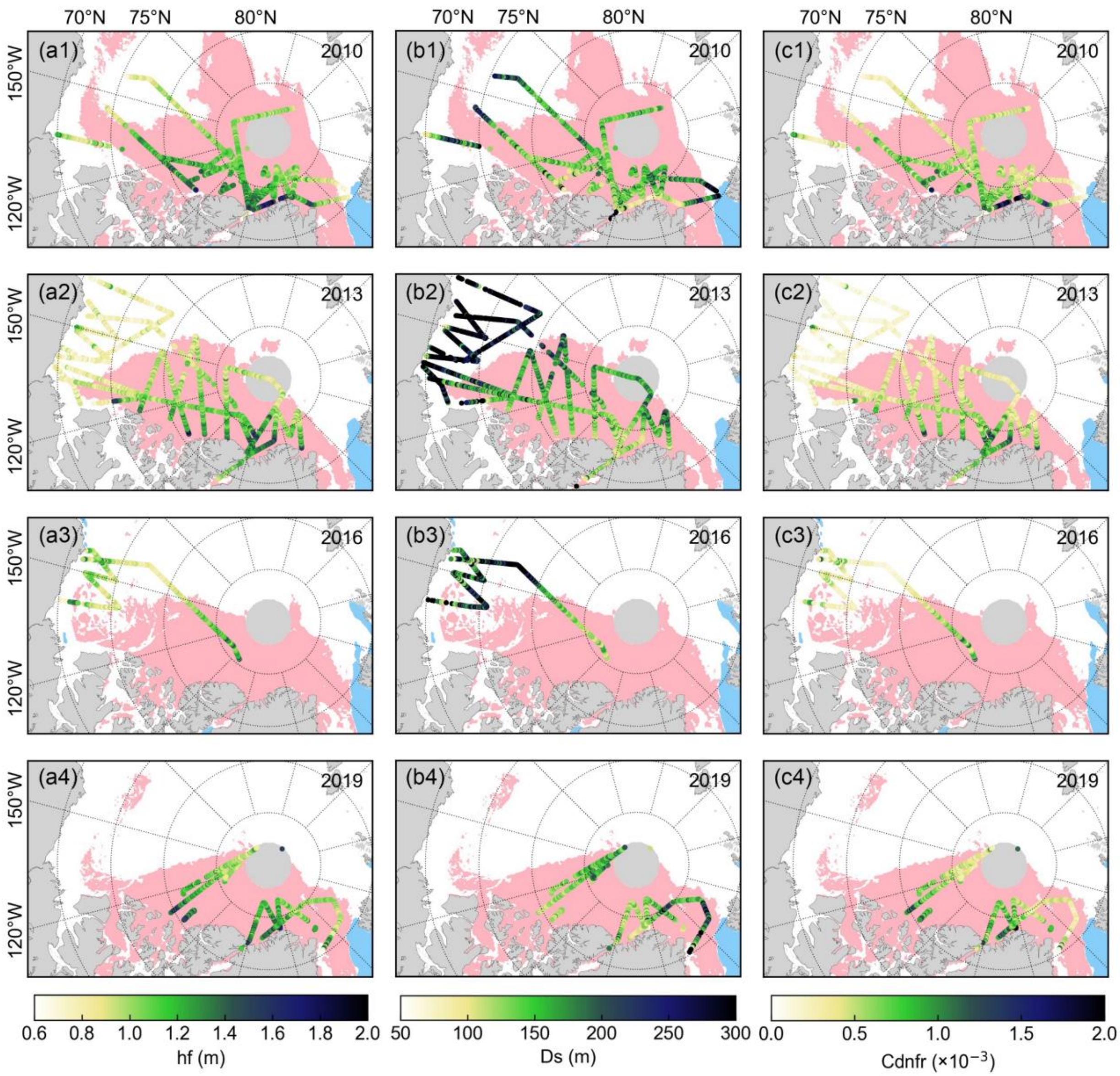

Fig. 7. Maps of the OIB-based 10-km mean (a) h_f, (b) D_s, and (c) $C_{dn,fr}$ in the late winter (March and April) of 2010, 2013, 2016, and 2019. The pink, white, and blue denote MYI, FYI, and open water, respectively.

B. Spatio-temporal variation of the scatterometer-based surface form drag coefficients over the entire Arctic

Fig. 8 and 9 shows the maps of the monthly mean $C_{dn,fr}$ in December and March based on the scatterometer-derived method. Generally speaking, the central Arctic has a larger $C_{dn,fr}$ than the surrounding seas, and the closer to north Greenland and the CAA, the higher the $C_{dn,fr}$. In March, the $C_{dn,fr}$ over MYI usually ranges from 0.4 to 2.0 × 10^{-3}, with a maximum over 2.0 × 10^{-3} in certain years (e.g., 2007 and 2015). In contrast, the $C_{dn,fr}$ is generally lower than 0.5 × 10^{-3} over FYI. These patterns are consistent with those from the OIB-based $C_{dn,fr}$. An increase of $C_{dn,fr}$ can be seen from early winter (December) to late winter (March), especially in the central Arctic and the marginal seas (Fig. 8 and 9). The reasons for the increased $C_{dn,fr}$ in the central Arctic during the winter season may include the accumulation and redistribution of snow [67], the growth in sea ice thickness, and the formation of pressure or shear ridges [31]. For the marginal seas, the interaction between the level young ice and waves can intensify the surface deformation of the ice cover, and hence the increase in $C_{dn,fr}$ [68]. There also appears to be a tendency for lower $C_{dn,fr}$ in the later years than in the early years.

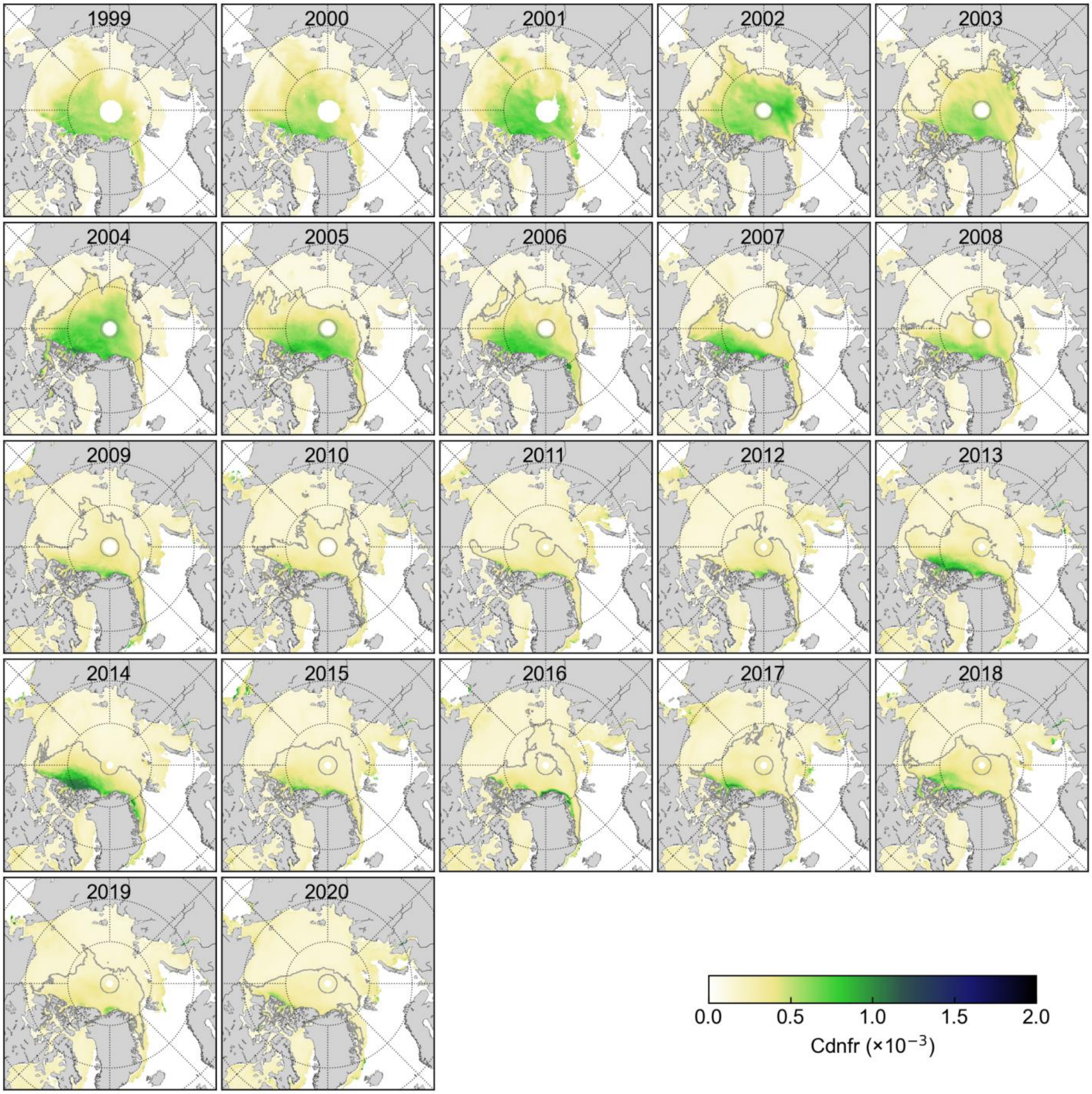

Fig. 8. Maps of monthly mean $C_{dn,fr}$ for December each year derived from the proposed method using QSCAT (1999–2009) and ASCAT (2009–2021) data. Only areas with a sea ice concentration greater than 90% are shown. The gray solid lines denote the MYI extent (2002–2020).

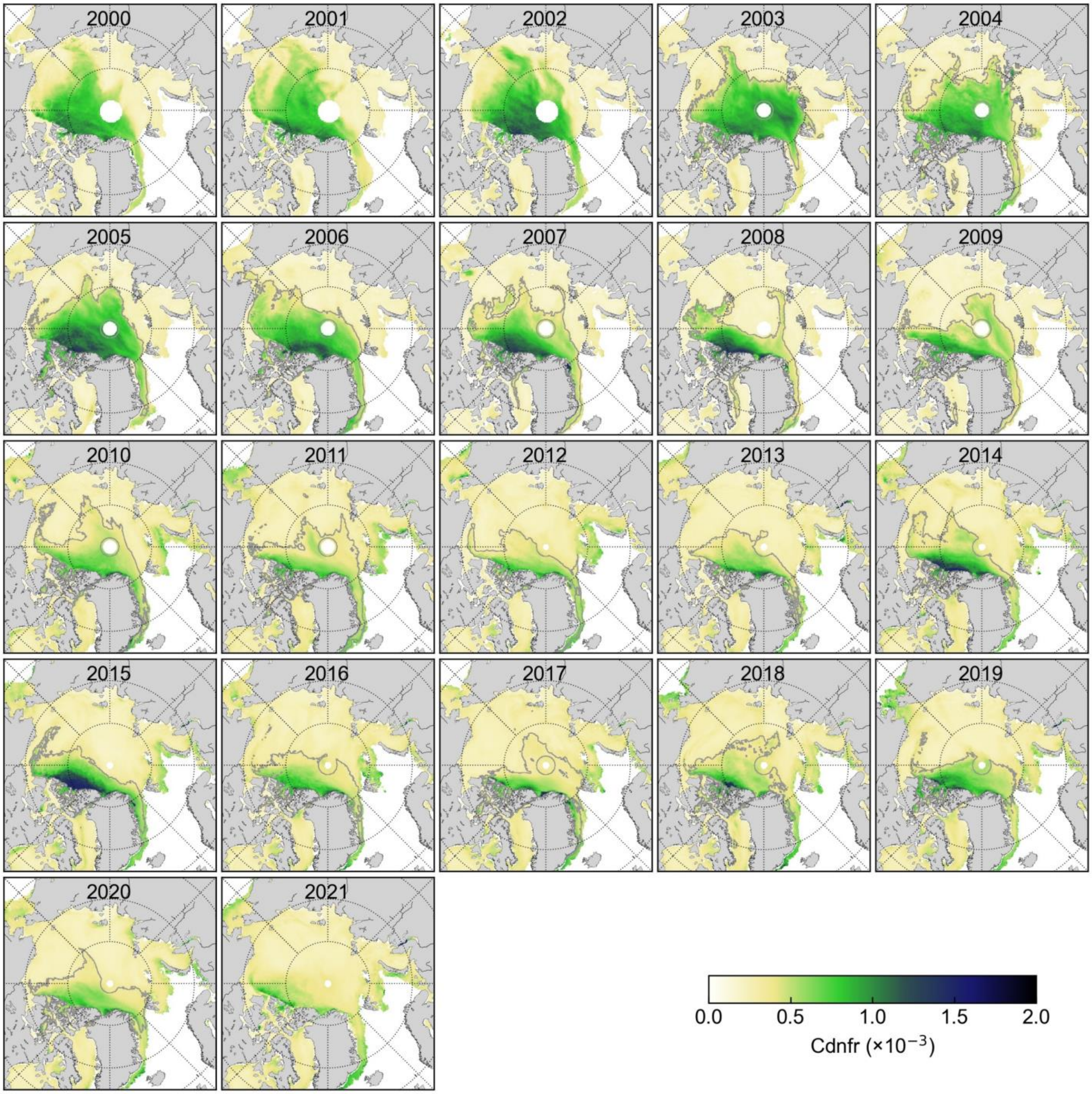

Fig. 9. Same as Fig. 8, but for March.

The time series of the monthly mean $C_{dn,fr}$ from QSCAT and ASCAT are shown in Fig. 10a, along with the OIB-based results. The QSCAT-based $C_{dn,fr}$ shows good continuity with that from ASCAT in terms of magnitude and trend (difference less than 13%). The differences mainly appear in the marginal seas (the reason for this is discussed later). The OIB-based $C_{dn,fr}$ shows similar trends to the scatterometer-based $C_{dn,fr}$ in March and April, but is ~30% higher. This is mainly due to the fact that the OIB results only cover the central and western Arctic, where the thicker and more deformed MYI dominates. During 1999–2021, the mean $C_{dn,fr}$ for the total Arctic sea ice cover (areas north of 60°N were counted) was 0.2–0.3 × 10^{-3} in early winter and increased to 0.5–0.6 × 10^{-3} by the end of winter. In April, the largest $C_{dn,fr}$ appeared in 2002 (0.52 × 10^{-3}), while the minimum was in 2013 (0.37 × 10^{-3}). The winter of 2008/2009 was an important turning point for $C_{dn,fr}$ as, since then, the April mean $C_{dn,fr}$ has remained below 0.40 × 10^{-3}. The record low values of $C_{dn,fr}$ in 2007 and 2013 were coupled with the rapid loss of sea ice extent, thickness, and MYI coverage in these two years [1, 3].

This article has been accepted for publication in IEEE Transactions on Geoscience and Remote Sensing. This is the author's version which has not been fully edited and content may change prior to final publication. Citation information: DOI 10.1109/TGRS.2023.3347694

According to the NSIDC region mask (https://nsidc.org/data/nsidc-0780/versions/1) (Fig. 9b), the interannual and seasonal variability of the scatterometer-based $C_{dn,fr}$ in eight sub-regions is illustrated in Fig. 10c–j. In the central Arctic (CA, Fig. 10c), a consistent decrease of $C_{dn,fr}$ took place from 2001/2002 to 2008/2009, from ~0.6 × 10^{-3} to ~0.3 × 10^{-3}. From 2009, the $C_{dn,fr}$ remained stable at ~0.3 × 10^{-3}, except for a moderate increase during 2014–2015. The increase is likely related to the strong convergence of sea ice along the coasts of Greenland and the CAA [29, 69], which is consistent with the spatial pattern of $C_{dn,fr}$ during December 2013–March 2015 (Fig. 8 and 9). A large increase of $C_{dn,fr}$ (~0.3 × 10^{-3}) can be seen during the winter months in the CA. In the BCS (Fig. 10d), $C_{dn,fr}$ shows a moderate interannual variability (0.2–0.3 × 10^{-3}) and seasonal increase (~0.2 × 10^{-3}). The relatively stable $C_{dn,fr}$ between years can be attributed to the Beaufort Gyre constraining the outflow of sea ice in the BCS. The $C_{dn,fr}$ in the East Siberian Sea and Laptev Sea (ESLS, Fig. 10e) is low (<0.2 × 10^{-3}) and stable between years, with a slight increase during the winter months. In the ESLS, the level and compact FYI dominates in winter, and thus a lower $C_{dn,fr}$ can be expected. For the Kara Sea and Barents Sea (KBS, Fig. 10f) and other marginal seas, e.g., Hudson Bay and Baffin Bay (HBB, Fig. 10h) and the Bering Sea (BS, Fig. 10j), the $C_{dn,fr}$ is relatively stable (0.2–0.4 × 10^{-3}), with only a moderate increase during the winter months (~0.15 × 10^{-3}). Significant differences can be observed between the QSCAT and ASCAT results (~30%) during the overlapping period (2006/2007–2008/2009) in the marginal seas. These differences mostly result from the higher σ_{vv}^{o} of ASCAT than QSCAT. Previous studies [40, 70] have shown that the C-band ASCAT is much more sensitive to surface scattering from deformed young ice in marginal seas than the Ku-band QSCAT, leading to a higher σ_{vv}^{o}. Moreover, for the proposed σ_{vv}^{o}-$C_{dn,fr}$ regression model it is difficult to reduce the biases in the marginal seas because the training data (OIB-based $C_{dn,fr}$) mainly covers the central Arctic and Beaufort Sea. The East Greenland Sea (EGS) shows a large increase of $C_{dn,fr}$ during winter (~0.3 × 10^{-3}), with strong interannual variability fluctuating around 0.3–0.7 × 10^{-3}. The variability in $C_{dn,fr}$ is linked to the ice conditions (e.g., type and deformation) exported out through the Fram Strait, forced by the Transpolar Drift Stream (TDS). In the CAA, the $C_{dn,fr}$ features moderate interannual variability (0.2–0.4 × 10^{-3}) and a large seasonal increase (~0.3 × 10^{-3}). The $C_{dn,fr}$ is likely affected by the amount of thick and deformed MYI entering into the land-fast ice coverage through the northern gates of the CAA.

This article has been accepted for publication in IEEE Transactions on Geoscience and Remote Sensing. This is the author's version which has not been fully edited and content may change prior to final publication. Citation information: DOI 10.1109/TGRS.2023.3347694

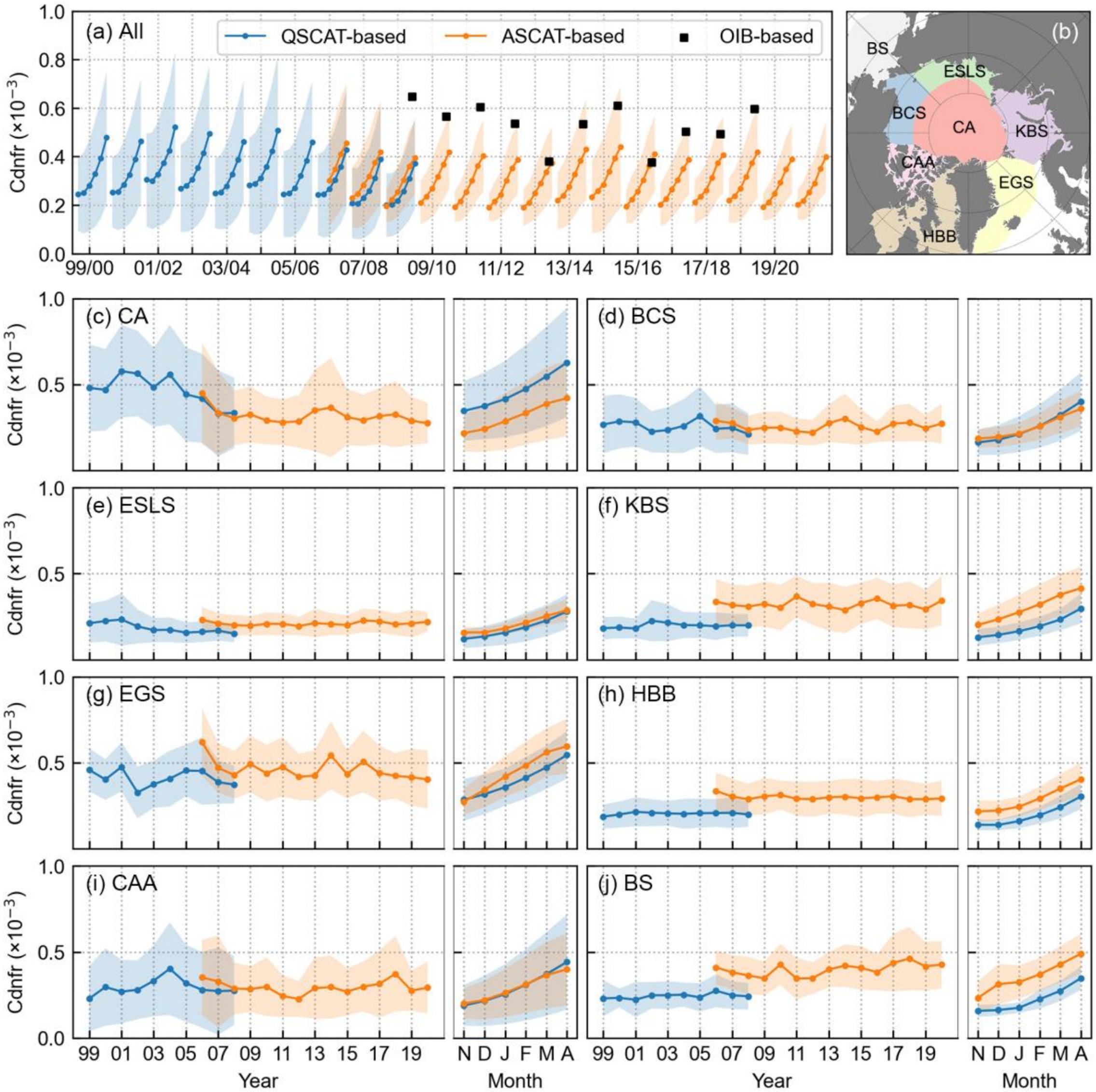

Fig. 10. (a) Mean $C_{dn,fr}$ from the scatterometer-based calculation for the winter months (November to following April) during 1999–2021 over Arctic sea ice (areas north of 60°N were counted). The shaded envelopes denote ± standard deviation. The winter (March–April) mean $C_{dn,fr}$ from the OIB ATM data (this study) and that from ASCAT (P2017) are also shown. (b)–(i) Annual mean and monthly mean in eight sub-regions: Central Arctic (CA), Beaufort and Chukchi seas (BCS), East Siberian Sea and Laptev Sea (ESLS), Kara Sea and Barents Sea (KBS), East Greenland Sea (EGS), Hudson Bay and Baffin Bay (HBB), Canadian Arctic Archipelago (CAA), and Bering Sea (BS).

C. Linkages to sea ice thickness and deformation

Despite the known feedback as the deformation (convergence) causes a mechanical increase of the ice thickness [71], the question on how this affects the air-sea ice surface drag is still unresolved. We therefore investigated the correlation of the interannual variability in $C_{dn,fr}$ with sea ice thickness and deformation during 1999–2021. The daily Arctic sea ice thickness was taken from PIOMAS. Based on the daily Arctic sea ice motion from NSIDC, the deformation of each grid cell (*i, j*) can be calculated as the velocity change per unit length (modified from Kimura and Wakatsuchi [72]):

$$\dot{V}_{i,j} = -\left[\frac{u\left(i+\frac{1}{2},j\right)-u\left(i-\frac{1}{2},j\right)}{dist}+\frac{v\left(i,j+\frac{1}{2}\right)-v\left(i,j-\frac{1}{2}\right)}{dist}\right] \quad (6)$$

where u and v are the drift components in the x- and y-directions, and *dist* is the grid resolution (25 km). The unit of deformation is per day (d^{-1}). The positive (negative) value means convergence (divergence) of sea ice and hence enhanced (reduced) deformation.

The analysis was conducted for two periods: the winters (November to the following April) in 1999–2008 and 2009–2021. The reasons for selecting these two periods were: 1) distinct trends of $C_{dn,fr}$ can be observed between the two

This article has been accepted for publication in IEEE Transactions on Geoscience and Remote Sensing. This is the author's version which has not been fully edited and content may change prior to final publication. Citation information: DOI 10.1109/TGRS.2023.3347694

periods; and 2) to avoid the impact of the bias between the QSCAT- and ASCAT-based $C_{dn,fr}$ on the long-term trend analysis. Fig. 11a–c shows the trend of the winter mean $C_{dn,fr}$, deformation, and thickness during the two periods. During 1999–2008, the $C_{dn,fr}$ showed a significant declining trend in the central and western Arctic (>0.03 × 10^{-3} yr^{-1}, Fig. 11a1). A large reduction in thickness happened in the Arctic Ocean, especially for the Pacific sector (Fig. 11b1). The deformation was enhanced mainly in the Beaufort Sea and the Nordic seas (Fig. 11c1). The variability in $C_{dn,fr}$ is positively correlated with sea ice thickness in the Arctic Ocean ($R > 0.6$, Fig. 11d1), but has a negative correlation in the marginal seas (e.g. the Kara Sea and Barent Sea). A possible reason is that with the thinning of Arctic sea ice, in the marginal seas, the strength of sea ice weakens and more deformation occurs [73], resulting in more ridges and rafts [74]. Besides, the increasing wind speed over Arctic sea ice may intensify snow redistribution [75, 76], producing more snow dunes. However, these features are likely less high than over multi-year ice, the increase in their density (decrease in spacing) will still contribute to an increase in $C_{dn,fr}$. The correlation between $C_{dn,fr}$ and deformation is not uniform across the Arctic Ocean, with positive correlation in the regions affected by the TDS (Fig. 11e1). In contrast, during 2009–2021, the rate of decrease of $C_{dn,fr}$ slowed down for the central Arctic, and the $C_{dn,fr}$ slightly increased in the marginal seas (Fig. 11a2). Meanwhile, the reduction of sea ice thickness decelerated (Fig. 11b2). The pattern of the deformation trend was almost the opposite to that of the last period (Fig. 11c2). $C_{dn,fr}$ is still positively correlated with sea ice thickness in the central Arctic (Fig. 11d2), but for the marginal seas (e.g., the Nordic seas), deformation tends to better correlate with $C_{dn,fr}$ (Fig. 11e2).

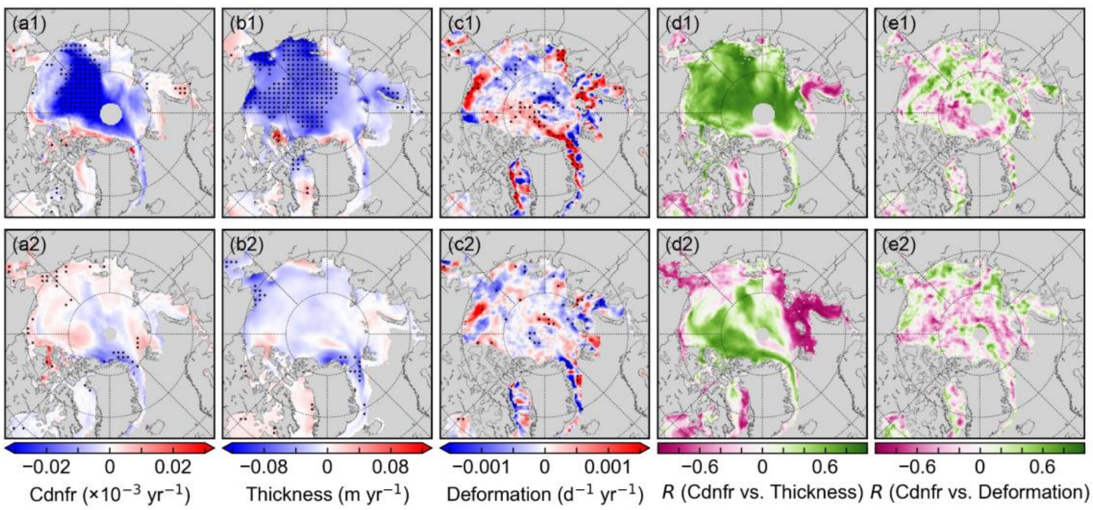

Fig. 11. Trends in the winter mean (a) $C_{dn,fr}$, (b) sea ice thickness, and (c) sea ice deformation, and the correlation coefficient of $C_{dn,fr}$ with (d) thickness and (e) deformation during (a1)–(e1) 1999–2008 and (a2)–(e2) 2009–2021. The dots represent areas with statistically significant trends ($p < 0.05$) (subsampled every five points).

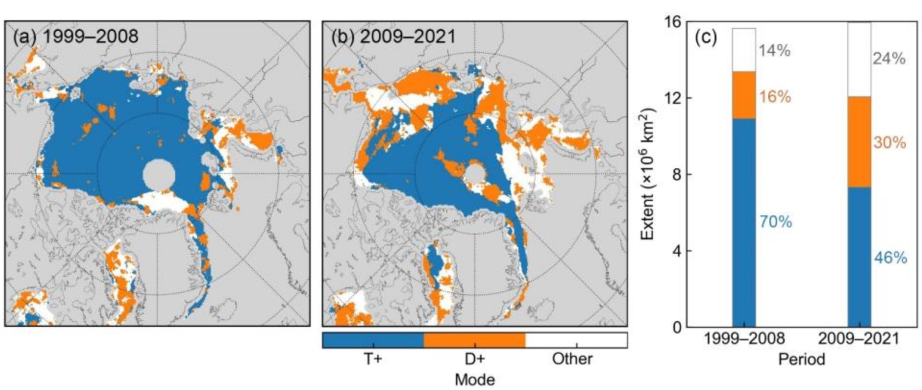

Fig. 12. Regions with different modes driving the interannual variability in $C_{dn,fr}$ during the winters of (a) 1999–2008 and (b) 2009–2021, with (c) the corresponding extents. "T+" denotes $C_{dn,fr}$ being mainly affected by sea ice thickness; "D+" denotes $C_{dn,fr}$ being mainly affected by deformation; "Other" denotes $C_{dn,fr}$ being mainly affected by other factors.

Furthermore, by comparing the correlation coefficient of $C_{dn,fr}$ with sea ice thickness and deformation, we defined three modes driving the interannual variability in $C_{dn,fr}$, namely T+ mode, D+ mode, and other mode (Fig. 12). "T+" represents $C_{dn,fr}$ being mainly affected by thickness, while "D+" denotes $C_{dn,fr}$ being mainly affected by deformation.

Regions where sea ice thickness and deformation were negatively correlated with $C_{dn,fr}$ were defined as the other mode. During 1999–2008, regions with the T+ mode dominated the Arctic sea ice (70%), while the D+ mode only covered marginal seas, e.g., the Kara Sea and Baffin Bay. However, since 2009, when the Arctic sea ice regime had already shifted into a thinner ice cover two years prior [3], almost all the marginal seas switched from T+ mode to D+ mode (e.g., the Laptev Sea and East Siberian Sea). The proportion of D+ mode nearly doubled, while the coverage of T+ mode shrank to 46%. This indicates an increasingly important role of deformation to $C_{dn,fr}$ over the young ice in the marginal seas in recent decades.

V. Discussion

A. Effect of the Rayleigh criterion and minimum interval distance on the identification of surface features

As introduced in Section III-B, a minimum separation interval of 10 m was required when searching the local maxima for each feature. For Petty, et al. [30], a distance of 25 m was actually used, according to their data processing scripts [http://www.github.com/akpetty/ibtopo2016.git]. To investigate the effect of the minimum interval distance and the Rayleigh criterion on the surface feature identification, we conducted four groups of experiments (Table V). Both group 1 and group 2 used a minimum interval distance of 10 m, while for group 3 and group 4, the distance was 25 m. Meanwhile, the Rayleigh criterion was applied in group 1 and group 3.

TABLE V
DETAILS OF THE FOUR GROUPS USING DIFFERENT SETTINGS OF RAYLEIGH CRITERION AND MINIMUM INTERVAL DISTANCE.

Group	Abbreviation	Applying Rayleigh criterion	Minimum interval distance
1	D10_with_RC	Yes	10 m
2	D10_no_RC	No	10 m
3	D25_with_RC	Yes	25 m
4	D25_no_RC	No	25 m

Fig. 13 shows the 10-km mean number of identified features and the mean values of h_f, D_s, and $C_{dn,fr}$ from the four groups, compared with the results from P2017. The results show that, with a minimum interval distance of 10 m, the number of features identified is reduced by 50% when the Rayleigh criterion is applied (Fig. 13a). In this case, the over-segmentation of the surface features is mitigated, as indicated by the "pseudo" local maxima shown in Fig. 2e–f (black points). When the minimum interval distance is increased to 25 m, the effect of the Rayleigh criterion on the identified features becomes insignificant, since most of the small features are already filtered out under this distance. When applying the Rayleigh criterion, ~30% more features are identified when using the distance of 10 m, compared to 25 m. The above findings confirm that the minimum interval distance of 10 m and the Rayleigh criterion (i.e., D10_with_RC) are the optimum settings for surface feature identification using OIB ATM data. These settings ensure that enough features are identified, while avoiding over-segmentation.

The mean values of h_f, D_s, and $C_{dn,fr}$ from the four groups agree well with each other in trends. Taking group 1 (D10_with_RC) as the base, group 2 (D10_no_RC) is 5% less for h_f, 23% less for D_s, and 28% larger for $C_{dn,fr}$, due to more "pseudo" features being identified. In contrast, group 3 (D25_with_RC) is 3% larger, 15% larger, and 11% less for h_f, D_s, and $C_{dn,fr}$, respectively. This is because only larger features are kept when a minimum distance of 25 m is used. Group 4 (D25_no_RC) has the same setting for the minimum distance as that used in P2017. The results from group 4 are comparable to those from P2017, with 8% less in h_f, 2% larger in D_s, and 19% less in $C_{dn,fr}$. The differences in $C_{dn,fr}$ mainly come from h_f, which is likely caused by the different interpolation methods when gridding the ATM data. As shown in Fig. S1, although the surface elevations based on the two interpolation methods are almost identical, h_f derived using the bilinear-interpolated data (i.e., this study) is 9% lower than that obtained using the linear-interpolated data (as used in P2017). We speculate that the bilinear interpolation is more appropriate because the ATM points from the four surrounding orthogonal directions are involved in the interpolation for each grid cell.

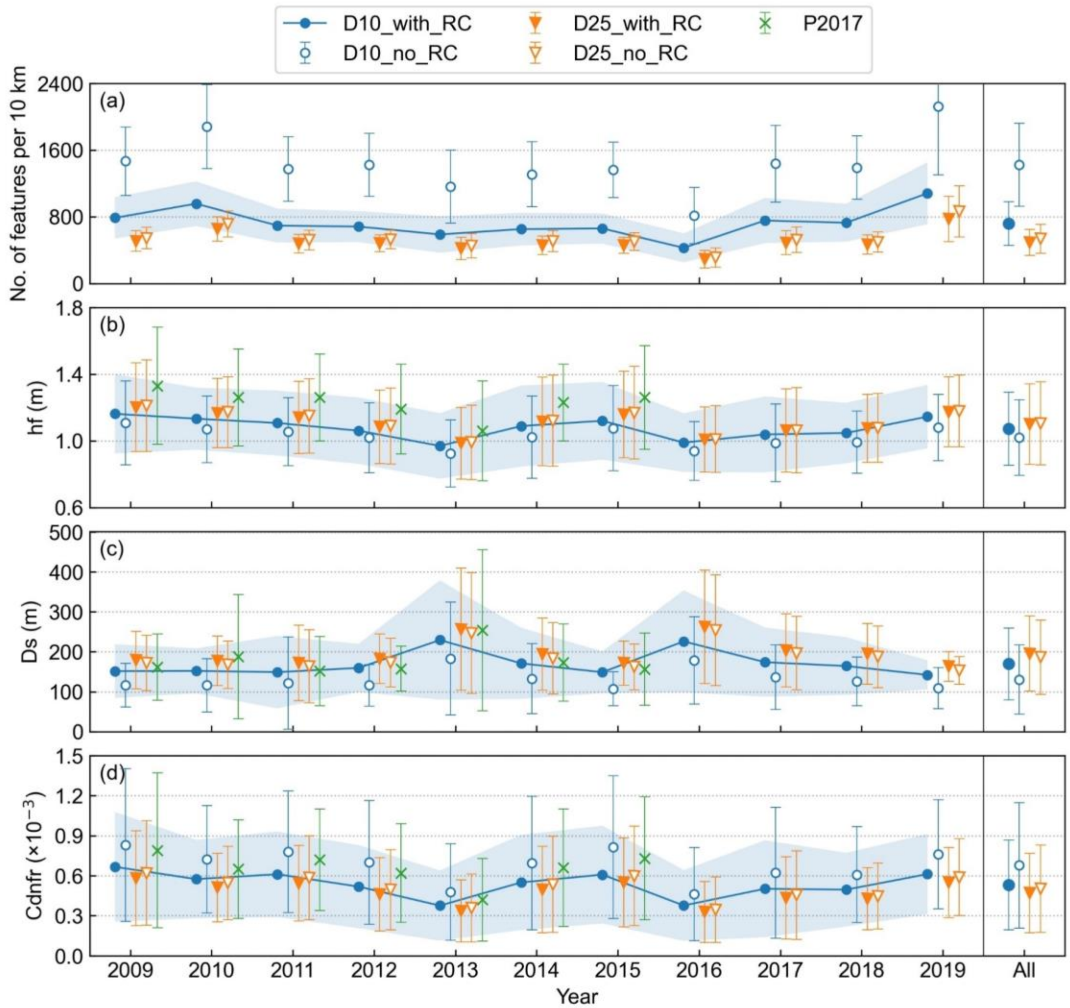

Fig. 13. Annual mean (a) number of identified features per 10 km, (b) 10-km mean h_f, (c) 10-km mean D_s, and (d) 10-km mean $C_{dn,fr}$ from the results obtained using different settings for the surface feature detection method. "D10_with_RC" ("D25_with_RC") denotes using the minimum interval distance of 10 m (25 m) and applying the Rayleigh criterion; "D10_no_RC" ("D25_no_RC") denotes using the minimum interval distance of 10 m (25 m) but without using the Rayleigh criterion. The shaded envelopes and the error bar indicate ± standard deviation.

B. Comparison with drag coefficient from other satellite observations and in-situ measurements

Two satellite-based surface drag coefficient datasets are available for the Arctic sea ice, one from P2017 and the other from M2023. In the two studies, the surface features (height > 0.2 m) were first extracted from OIB ATM data for the late winter and used to calculate $C_{dn,fr}$ in 10-km segments. The OIB-based $C_{dn,fr}$ was then taken as the training data in both studies, among which P2017 estimated the daily Arctic $C_{dn,fr}$ from ASCAT during March and April of 2009–2015, while M2023 derived the monthly composite Arctic $C_{dn,fr}$ by scaling up the $C_{dn,fr}$ derived from ICESat-2 elevation data from November 2018 to May 2022. Using the drag parameterization from Lüpkes, et al. [24], both studies obtained the total drag coefficients over Arctic sea ice. To compare the results obtained in this study with P2017 and M2023, we calculated the total drag coefficient (C_{dn}) over Arctic sea ice using the same drag parameterization of Lüpkes, et al. [24], as follows:

$$C_{dn} = (1 - A)C_{dn,ow} + AC_{dn,i} + C_{dn,fe} + AC_{dn,fr} \quad (7)$$

where A is the sea ice concentration from passive microwave observations, $C_{dn,ow}$ is the drag of open water (1.5×10^{-3}), $C_{dn,i}$ is the skin drag of sea ice (0.84×10^{-3}), $C_{dn,fe}$ is the form drag due to the ice edge ($3.67 \times 10^{-3}A(1\text{-}A)$), and $C_{dn,fr}$ is the form drag due to the surface features derived from QSCAT and ASCAT. It should be noted again that $C_{dn,fr}$ was only considered for regions with sea ice concentration over 90%. Figure S5 shows that $C_{dn,fr}$ dominates the form drag in the compact ice region while $C_{dn,fe}$ dominates the marginal ice zone. An example of the map of $C_{dn,fr}$, $C_{dn,fe}$, and C_{dn} for the winter of 2014/2015 is illustrated in Figure S6. The monthly mean C_{dn} for December and March during 1999–2021 are shown in Figure S7 and S8, respectively.

TABLE VI
COMPARISON OF C_{dn} OF BETWEEN IN-SITU MEASUREMENTS AND SCATTEROMETER-BASED ESTIMATES.

Campaign	Overlapped period & location	Number of days	In-situ measured C_{dn} (Mean ± S.D., $\times 10^{-3}$)	Scatterometer-based C_{dn} (Mean ± S.D., $\times 10^{-3}$)
N-ICE2015	Jan.–Apr. 2015 North of Svalbard	34	1.22 ± 0.58	1.15 ± 0.08
MOSAiC	Nov. 2019–Apr. 2020 Central Arctic to Fram Strait	82	1.17 ± 0.37	1.00 ± 0.02

Note: S.D. denotes standard deviation

We compared the time series of C_{dn} from P2017 and M2023 with the results obtained in this study (Fig. 14). For March and April, the results obtained in this study show an interannual variability that is similar to the P2017 results, with the difference less than 4%. The bias between the two results may have been caused by the different values and temporal coverage of the OIB-based $C_{dn,fr}$ used for training the regression model (as shown in Section V-A). The results obtained in this study generally agree with those from M2023 in terms of magnitude and seasonal and interannual trends. However, M2023 is 10% higher than the results obtained in this study, with the smallest bias in December (5%) and the largest bias in April (14%). The causes of the differences between the results may be complicated because of the different satellite sensors (microwave scatterometer vs. laser altimeter) and retrieval methods used (σ_{vv}^{o} - σ_h - $C_{dn,fr}$ regression vs. scale-up of $C_{dn,fr}$). One possible reason may be the different dimensions selected (2-D vs. 1-D) to extract surface features from the OIB ATM data. The surface features were extracted using 2-D scanning elevation data in this study, while M2023 used 1-D profile data. As indicated in P2017, the $C_{dn,fr}$ calculated from the 1-D profiles is ~19% higher than that from the 2-D scanning data using the same ATM data. Thus, the bias between the two sets of OIB-based $C_{dn,fr}$ may be propagated to the pan-Arctic $C_{dn,fr}$ estimates through the regression process. Overall, the proposed method is closer to the idea of P2016 and P2017, thus it is clear that the differences between P2017 results and ours are smaller than those between M2023 results and ours.

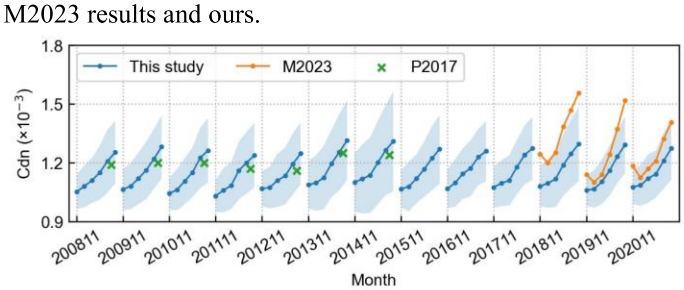

Fig. 14. Comparison of the monthly mean $C_{dn,fr}$ from this study (ASCAT-based), M2023 (ICESat-2-based), and P2017 (ASCAT-based). The P2017 results are averages from March and April. Note that the y-axis starts from 0.9×10^{-3}.

Moreover, we compared the satellite-based C_{dn} with in-situ measurements from two sea ice campaigns, namely the Norwegian Young Sea Ice Cruise (N-ICE2015, January–June 2015) [77] and the Multidisciplinary drifting Observatory for the Study of Arctic Climate (MOSAiC, September 2019–October 2020) [78] (Table VI). Measurements from the Met City were selected for MOSAiC. Only the overlapped wintertime period between the satellite observations and in-situ measurements were considered. The in-situ measured C_{dn} were averaged into daily means and compared with the nearest grid cell of the satellite-based C_{dn}. In general, our new C_{dn} dataset is comparable to the N-ICE2015 and MOSAiC measurements, with a slight underestimation of 6% and 15%, respectively. Besides, C_{dn} from the satellite observations shows fewer temporal variabilities (smaller standard deviation) than that from in-situ measurements. This could be explained by the difference of spatial scale. The satellite-based C_{dn} represents the mean value within 12.5 km ×12.5 km grid cell while in-situ observations reflect the local surface conditions around the observatories.

C. Improvements, limitations, and perspectives

The highlights of this study include: 1) an improved surface feature detection algorithm that solves the problem of over-segmentation of surface features from OIB ATM data; 2) the novel σ_{vv}^{o} - σ_h - $C_{dn,fr}$ regression model that extrapolates $C_{dn,fr}$ to the entire winter season using QSCAT and ASCAT backscatter observations; and 3) the time series of wintertime daily Arctic sea ice $C_{dn,fr}$ with the longest record (1999–2021) so far. The $C_{dn,fr}$ estimates have been shown to be reliable and robust, compared to previous estimates from OIB ATM [30], ASCAT [30], and ICESat-2 [32]. From an observational perspective, this study has revealed the spatio-temporal variability of $C_{dn,fr}$ over the last 20 years for the first time and also demonstrated the increasing contribution of sea ice deformation to $C_{dn,fr}$ since 2009.

Nevertheless, limitations still exist, e.g., the scatterometer-based $C_{dn,fr}$ is unavailable for summer because sea ice surface melt confuses the interpretation of σ_{vv}^{o}. Furthermore, the inconsistency between the QSCAT and ASCAT estimates in the marginal seas, due to their frequency difference, was not addressed. In the future, direct measurements of the surface features (and hence $C_{dn,fr}$) from ICESat-2 [31, 32] could serve as a complement to the scatterometer-based $C_{dn,fr}$ in

This article has been accepted for publication in IEEE Transactions on Geoscience and Remote Sensing. This is the author's version which has not been fully edited and content may change prior to final publication. Citation information: DOI 10.1109/TGRS.2023.3347694

the summer, while supporting the optimization of the σ_{vv}^{o}-σ_h-$C_{dn,fr}$ regression model over a wider range of time and space than the OIB ATM data. Moreover, the latest in-situ and airborne measurements of Arctic sea ice surface topography and drag coefficient can be expected to validate and improve the satellite-based drag coefficient estimates, e.g., the helicopter laser scanning data obtained during the Multidisciplinary drifting Observatory for the Study of Arctic Climate (MOSAiC) expedition [33]. Furthermore, by considering the stability of the lower atmosphere (e.g., Lüpkes and Gryanik [25]), the pan-Arctic $C_{dn,fr}$ will support the estimation of total drag and transfer coefficients across the Arctic sea ice (and hence the turbulent fluxes of momentum and heat), offering new insights into the dynamic and thermodynamic air-ice interactions in response to the changing climate and sea ice in the Arctic. The new $C_{dn,fr}$ dataset could also refine the Arctic ocean and sea ice modeling, in which the form drag is currently poorly accounted for and significantly affects the simulation of boundary layer properties such as surface winds, sea ice thickness, and sea surface salinities [79, 80].

VI. Conclusions

The main objective of this study was to obtain a long-term record of wintertime pan-Arctic sea ice neutral form drag coefficient ($C_{dn,fr}$) due to surface features (obstacles with a height over 20 cm) and investigate its spatio-temporal variability over the last 20 years. We first improved the surface feature algorithm developed in Petty, et al. [29] by incorporating the Rayleigh criterion, which ensures that enough surface features are identified while avoiding over-segmentation. Based on the improved algorithm, the sea ice surface features (including height and spacing) were characterized in 10-km segments using the full-scan elevation data from the ATM instrument obtained during the OIB missions (central and western Arctic, March/April 2009–2019). $C_{dn,fr}$ was then calculated from the surface feature height and spacing, using the parameterization scheme from Garbrecht, et al. [27]. Finally, an integrated backscatter-roughness-$C_{dn,fr}$ regression model was developed to extrapolate the OIB-based $C_{dn,fr}$ to the pan-Arctic scale for the entire winter season and over two decades (1999–2021), using the backscatter coefficients from QuikSCAT and ASCAT, assisted by the sea ice surface roughness from ICESat and ICESat-2.

During the OIB period, the surface features had an average (± standard deviation) height, spacing, and $C_{dn,fr}$ of 1.07 ± 0.22 m, 171 ± 94 m, and 0.53 ± 0.34 × 10^{-3}, respectively. The feature height and form drag coefficient from all the years follow a log-normal distribution, while the long tail of the feature spacing is close to an exponential distribution. Higher and denser surface features are more common over MYI than FYI, especially north of Greenland.

The largest $C_{dn,fr}$ was found in the central Arctic and north of Greenland (with a maximum > 2 × 10^{-3}) and a small $C_{dn,fr}$ was found in the surrounding seas (< 0.5 × 10^{-3}). $C_{dn,fr}$ continuously increased throughout the winter months, nearly doubling from November to April. In terms of the interannual trend, the mean $C_{dn,fr}$ in the central Arctic was reduced by 50% in the period from 2001/2002 to 2008/2009 and has thereafter stayed at around 0.3 × 10^{-3}. The marginal seas showed low and moderate variability during 1999–2021, with no significant trends. Both the sea ice thickness and deformation were closely linked to the interannual variability in $C_{dn,fr}$, but with discrepant correlations in space and time. In the central Arctic, the loss (gain) in sea ice thickness accounted for most of the decrease (increase) in $C_{dn,fr}$, while deformation was a leading factor for $C_{dn,fr}$ in the marginal seas. Notably, sea ice thickness dominated the changes in $C_{dn,fr}$ in most regions before 2008, whereas deformation became increasingly important since 2009, when the Arctic sea ice had already turned into a more rapidly moving and thinner regime [3].

By applying a total drag (C_{dn}) parameterization from Lüpkes, et al. [24], pan-Arctic C_{dn} was estimated for the winters of 1999–2021. The derived C_{dn} agreed well with in-situ measurements from N-ICE2015 and MOSAiC, with an underestimation of 6% and 15%, respectively. The new C_{dn} dataset were also consistent with other satellite-based estimates, e.g., ASCAT results [30] and ICESat-2 results [32] (differences < 4% and < 10%, respectively), highlighted with the longest record and daily wintertime observations. More validation and optimization of the scatterometer-based $C_{dn,fr}$ can be expected with the increasing availability of in-situ observations of Arctic sea ice topography. The scatterometer-based $C_{dn,fr}$ will support refined turbulent flux estimates over the Arctic sea ice from both satellite observations and modellings, and will shed light on the air-ice interactions in the Arctic with changed sea ice conditions.

Data availability

The IceBridge ATM L1B elevation data are available from https://nsidc.org/data/ilatm1b/versions/1 and https://nsidc.org/data/ilatm1b/versions/2. The IceBridge POS/AV L1B corrected position and attitude data are available from https://nsidc.org/data/ipapp1b/versions/1. The daily gridded QSCAT and ASCAT backscatter data are available from ftp://ftp.ifremer.fr/ifremer/cersat/products/gridded/psi-ackscatter/data/quickscat/arctic/ and ftp://ftp.ifremer.fr/ifremer/cersat/products/gridded/psi-ackscatter/data/ascat/arctic/, respectively. The daily gridded AMSR-E and AMSR2 brightness temperature data are available from https://seaice.uni-bremen.de/data/amsre/tb_daygrid_swath/ and https://seaice.uni-bremen.de/data/amsr2/tb_daygrid_swath/, respectively. The NT-based sea ice concentration data from SSM/I and SSMI/S are available from https://nsidc.org/data/nsidc-0051/versions/2. The ASI sea ice concentration from AMSR-E, SSMI/S, and AMSR2 are available from https://seaice.uni-bremen.de/data/amsre/asi_daygrid_swath/n6250/, https://seaice.uni-bremen.de/data/ssmis/asi_daygrid_swath/n6250/, and https://seaice.uni-bremen.de/data/amsr2/asi_daygrid_swath/n6250/, respectively. The sea ice type data are available from http://www.orsc.hellosea.org.cn/#/product-detail?ProductId=2. The GLAS/ICESat L2 sea ice altimetry data are available from https://nsidc.org/data/glah13/versions/34. The ATLAS/ICESat-2 L3A sea ice height data are available from https://nsidc.org/data/atl07/versions/5. The PIOMAS data are available from http://psc.apl.uw.edu/research/projects/arctic-sea-ice-volume-anomaly/data/model_grid. All the data used were last accessed on 1 March 2023. The QSCAT- and ASCAT-based Cdnfr estimates are available at https://doi.org/10.5281/zenodo.10421183 and https://doi.org/10.5281/zenodo.10421427, respectively.

DECLARATION OF COMPETING INTEREST

The authors declare no conflict of interest.

ACKNOWLEDGEMENT

The authors would like to thank the National Snow and Ice Data Center (NSIDC) for providing the OIB data, ICESat/ICESat-2 data, and ice motion data, the National Institute for Ocean Science (IFREMER) for providing the QuikSCAT and ASCAT data, the University of Bremen for providing the sea ice concentration data, and the University of Washington for providing the PIOMAS data.

REFERENCES

[1] R. Kwok, "Arctic sea ice thickness, volume, and multiyear ice coverage: losses and coupled variability (1958–2018)," (in English), *Environmental Research Letters,* vol. 13, no. 10, p. 105005, 2018.
[2] W. N. Meier and J. Stroeve, "An updated assessment of the changing Arctic sea ice cover," *Oceanography,* vol. 35, no. 3/4, pp. 10-19, 2022.
[3] H. Sumata, L. de Steur, D. V. Divine, M. A. Granskog, and S. Gerland, "Regime shift in Arctic Ocean sea ice thickness," *Nature,* vol. 615, no. 7952, pp. 443-449, 2023.
[4] A. C. Bliss, M. Steele, G. Peng, W. N. Meier, and S. Dickinson, "Regional variability of Arctic sea ice seasonal change climate indicators from a passive microwave climate data record," *Environmental Research Letters,* vol. 14, no. 4, p. 045003, 2019.
[5] L. Lin, R. Lei, M. Hoppmann, D. K. Perovich, and H. He, "Changes in the annual sea ice freeze–thaw cycle in the Arctic Ocean from 2001 to 2018," *The Cryosphere,* vol. 16, no. 12, pp. 4779-4796, 2022.
[6] G. Spreen, R. Kwok, and D. Menemenlis, "Trends in Arctic sea ice drift and role of wind forcing: 1992–2009," *Geophysical Research Letters,* vol. 38, no. 19, 2011.
[7] F. Zhang, X. Pang, R. Lei, M. Zhai, X. Zhao, and Q. Cai, "Arctic sea ice motion change and response to atmospheric forcing between 1979 and 2019," *International Journal of Climatology,* vol. 42, no. 3, pp. 1854-1876, 2022.
[8] P. Rampal, J. Weiss, and D. Marsan, "Positive trend in the mean speed and deformation rate of Arctic sea ice, 1979–2007," *Journal of Geophysical Research: Oceans,* vol. 114, no. C5, 2009.
[9] L. L. Landrum and M. M. Holland, "Influences of changing sea ice and snow thicknesses on simulated Arctic winter heat fluxes," *The Cryosphere,* vol. 16, no. 4, pp. 1483-1495, 2022.
[10] X. Li *et al.*, "Unprecedented Arctic sea ice thickness loss and multiyear-ice volume export through Fram Strait during 2010–2011," *Environmental Research Letters,* vol. 17, no. 9, p. 095008, 2022.
[11] A. Dai, D. Luo, M. Song, and J. Liu, "Arctic amplification is caused by sea-ice loss under increasing CO 2," (in English), *Nature communications,* vol. 10, no. 1, pp. 1-13, 2019.
[12] M. Jenkins and A. Dai, "The Impact of Sea‐Ice Loss on Arctic Climate Feedbacks and Their Role for Arctic Amplification," (in English), *Geophysical Research Letters,* vol. 48, no. 15, p. e2021GL094599, 2021.
[13] M. Previdi, K. L. Smith, and L. M. Polvani, "Arctic amplification of climate change: a review of underlying mechanisms," (in English), *Environmental Research Letters,* vol. 16, no. 9, p. 093003, 2021.
[14] M. Rantanen *et al.*, "The Arctic has warmed nearly four times faster than the globe since 1979," (in English), *Communications Earth & Environment,* vol. 3, no. 1, p. 168, 2022.
[15] M. C. Serreze and J. A. Francis, "The Arctic amplification debate," (in English), *Climatic change,* vol. 76, no. 3, pp. 241-264, 2006.
[16] W. D. Hibler, "A dynamic thermodynamic sea ice model," *Journal of physical oceanography,* vol. 9, no. 4, pp. 815-846, 1979.
[17] A. Thorndike and R. Colony, "Sea ice motion in response to geostrophic winds," *Journal of Geophysical Research: Oceans,* vol. 87, no. C8, pp. 5845-5852, 1982.
[18] E. Andreas, C. Paulson, R. William, R. Lindsay, and J. Businger, "The turbulent heat flux from Arctic leads," (in English), *Boundary-Layer Meteorology,* vol. 17, no. 1, pp. 57-91, 1979.
[19] G. A. Maykut, "Large‐scale heat exchange and ice production in the central Arctic," *Journal of Geophysical Research: Oceans,* vol. 87, no. C10, pp. 7971-7984, 1982.
[20] E. L. Andreas, "A theory for the scalar roughness and the scalar transfer coefficients over snow and sea ice," (in English), *Boundary-Layer Meteorology,* vol. 38, no. 1, pp. 159-184, 1987.
[21] E. L. Andreas, "Parameterizing scalar transfer over snow and ice: A review," *Journal of Hydrometeorology,* vol. 3, no. 4, pp. 417-432, 2002.
[22] S. Arya, "Contribution of form drag on pressure ridges to the air stress on Arctic ice," *Journal of Geophysical Research,* vol. 78, no. 30, pp. 7092-7099, 1973.
[23] S. Arya, "A drag partition theory for determining the large‐scale roughness parameter and wind stress on the Arctic pack ice," *Journal of Geophysical Research,* vol. 80, no. 24, pp. 3447-3454, 1975.
[24] C. Lüpkes, V. M. Gryanik, J. Hartmann, and E. L. Andreas, "A parametrization, based on sea ice morphology, of the neutral atmospheric drag coefficients for weather prediction and climate models," (in English), *Journal of Geophysical Research: Atmospheres,* vol. 117, no. D13, 2012.
[25] C. Lüpkes and V. M. Gryanik, "A stability‐dependent parametrization of transfer coefficients for momentum and heat over polar sea ice to be used in climate models," (in English), *Journal of Geophysical Research: Atmospheres,* vol. 120, no. 2, pp. 552-581, 2015.
[26] M. Tsamados *et al.*, "Impact of variable atmospheric and oceanic form drag on simulations of Arctic sea ice," *Journal of Physical Oceanography,* vol. 44, no. 5, pp. 1329-1353, 2014.
[27] T. Garbrecht, C. Lüpkes, J. Hartmann, and M. Wolff, "Atmospheric drag coefficients over sea ice–validation of a parameterisation concept," *Tellus A: Dynamic Meteorology and Oceanography,* vol. 54, no. 2, pp. 205-219, 2002.
[28] G. Castellani, C. Lüpkes, S. Hendricks, and R. Gerdes, "Variability of Arctic sea‐ice topography and its impact on the atmospheric surface drag," *Journal of Geophysical Research: Oceans,* vol. 119, no. 10, pp. 6743-6762, 2014.
[29] A. A. Petty *et al.*, "Characterizing Arctic sea ice topography using high-resolution IceBridge data," *The Cryosphere,* vol. 10, no. 3, pp. 1161-1179, 2016.
[30] A. A. Petty, M. C. Tsamados, and N. T. Kurtz, "Atmospheric form drag coefficients over Arctic sea ice using remotely sensed ice topography data, spring 2009–2015," (in English), *Journal of Geophysical Research: Earth Surface,* vol. 122, no. 8, pp. 1472-1490, 2017.
[31] K. Duncan and S. L. Farrell, "Determining Variability in Arctic Sea Ice Pressure Ridge Topography With ICESat‐2," *Geophysical Research Letters,* vol. 49, no. 18, p. e2022GL100272, 2022.
[32] A. Mchedlishvili, C. Lüpkes, A. Petty, M. Tsamados, and G. Spreen, "New estimates of the pan-Arctic sea ice–atmosphere neutral drag coefficients from ICESat-2 elevation data," *The Cryosphere,* vol. 17, no. 9, pp. 4103–4131, 2023.
[33] R. Ricker *et al.*, "Linking scales of sea ice surface topography: evaluation of ICESat-2 measurements with coincident helicopter laser scanning during MOSAiC," *The Cryosphere,* vol. 17, no. 3, pp. 1411-1429, 2023.
[34] K. Chikhar *et al.*, "Sensitivity of ice drift to form drag and ice strength parameterization in a coupled ice–ocean model," *Atmosphere-Ocean,* vol. 57, no. 5, pp. 329-349, 2019.
[35] J. A. MacGregor *et al.*, "The scientific legacy of NASA's Operation IceBridge," ed: Wiley Online Library, 2021.
[36] W. Krabill, "IceBridge ATM L1B Qfit elevation and return strength," *Boulder, Colorado USA: NASA DAAC at the National Snow and Ice Data Center,* vol. 10, 2010.
[37] W. Krabill, "IceBridge ATM L1B elevation and return strength, Version

2," *Boulder, Colorado USA: NASA DAAC at the National Snow and Ice Data Center,* 2013.

[38] W. Krabill, "IceBridge ATM L1B elevation and return strength," *Boulder, CO: NASA DAAC at the National Snow and Ice Data Center,* 2016.

[39] Z. Zhang, Y. Yu, X. Li, F. Hui, X. Cheng, and Z. Chen, "Arctic sea ice classification using microwave scatterometer and radiometer data during 2002–2017," (in English), *IEEE Transactions on Geoscience and Remote Sensing,* vol. 57, no. 8, pp. 5319-5328, 2019.

[40] Z. Zhang *et al.*, "Intercomparison of Arctic Sea Ice Backscatter and Ice Type Classification Using Ku-Band and C-Band Scatterometers," *IEEE Transactions on Geoscience and Remote Sensing,* vol. 60, pp. 1-18, 2021.

[41] M. Belmonte Rivas, I. Otosaka, A. Stoffelen, and A. Verhoef, "A scatterometer record of sea ice extents and backscatter: 1992–2016," *The Cryosphere,* vol. 12, no. 9, pp. 2941-2953, 2018.

[42] A. M. Swan and D. G. Long, "Multiyear Arctic sea ice classification using QuikSCAT," *IEEE Transactions on Geoscience and Remote Sensing,* vol. 50, no. 9, pp. 3317-3326, 2012.

[43] T. Lungu and P. Callahan, "QuikSCAT science data product user's manual: Overview and geophysical data products," *D-18053-Rev A, version,* vol. 3, p. 91, 2006.

[44] J. Figa-Saldaña, J. J. Wilson, E. Attema, R. Gelsthorpe, M. R. Drinkwater, and A. Stoffelen, "The advanced scatterometer (ASCAT) on the meteorological operational (MetOp) platform: A follow on for European wind scatterometers," *Canadian journal of remote sensing,* vol. 28, no. 3, pp. 404-412, 2002.

[45] R. G. Onstott and F. Carsey, "SAR and scatterometer signatures of sea ice," *Microwave remote sensing of sea ice,* vol. 68, pp. 73-104, 1992.

[46] M. Shokr and N. Sinha, *Sea ice: physics and remote sensing*. John Wiley & Sons, 2015.

[47] R. Kwok, H. J. Zwally, and D. Yi, "ICESat observations of Arctic sea ice: A first look," (in English), *Geophysical Research Letters,* vol. 31, no. 16, 2004.

[48] B. E. Schutz, H. J. Zwally, C. A. Shuman, D. Hancock, and J. P. DiMarzio, "Overview of the ICESat mission," *Geophysical Research Letters,* vol. 32, no. 21, 2005.

[49] S. Farrell, K. Duncan, E. Buckley, J. Richter‐Menge, and R. Li, "Mapping sea ice surface topography in high fidelity with ICESat‐2," (in English), *Geophysical Research Letters,* vol. 47, no. 21, p. e2020GL090708, 2020.

[50] R. Kwok *et al.*, "ATLAS/ICESat‐2 L3A sea ice height, version 1," *Boulder, Colorado USA. NSIDC: National Snow and Ice Data Center,* vol. 20, 2019.

[51] H. Zwally, R. Schutz, D. Hancock, and J. Dimarzio, "GLAS/ICESat L2 Sea Ice Altimetry Data (HDF5), Version 34," *Accessed: Jul,* vol. 20, p. 2020, 2014.

[52] D. J. Cavalieri, P. Gloersen, and T. T. Wilheit, "Aircraft and satellite passive microwave observations of the Bering Sea ice cover during MIZEX West," *IEEE transactions on geoscience and remote sensing,* no. 3, pp. 368-377, 1986.

[53] G. Spreen, L. Kaleschke, and G. Heygster, "Sea ice remote sensing using AMSR‐E 89‐GHz channels," (in English), *Journal of Geophysical Research: Oceans,* vol. 113, no. C2, 2008.

[54] D. Cavalieri *et al.*, "NASA Sea Ice Validation Program for the DMSP SSM/I: final report. NASA Technical Memorandum 104559, National Aeronautics and Space Administration," ed, 1992.

[55] M. Tschudi, W. Meier, J. Stewart, C. Fowler, and J. Maslanik, "Polar pathfinder daily 25 km EASE-grid sea ice motion vectors, version 4," *Boulder, CO: NASA National Snow and Ice Data Center Distributed Active Archive Center,* vol. 10, 2019.

[56] X. Wang, R. Chen, C. Li, Z. Chen, F. Hui, and X. Cheng, "An intercomparison of satellite derived Arctic sea ice motion products," *Remote Sensing,* vol. 14, no. 5, p. 1261, 2022.

[57] J. Zhang and D. A. Rothrock, "Modeling global sea ice with a thickness and enthalpy distribution model in generalized curvilinear coordinates," *Monthly Weather Review,* vol. 131, no. 5, pp. 845-861, 2003.

[58] A. Schweiger, R. Lindsay, J. Zhang, M. Steele, H. Stern, and R. Kwok, "Uncertainty in modeled Arctic sea ice volume," *Journal of Geophysical Research: Oceans,* vol. 116, no. C8, 2011.

[59] J. Stroeve, A. Barrett, M. Serreze, and A. Schweiger, "Using records from submarine, aircraft and satellites to evaluate climate model simulations of Arctic sea ice thickness," *The Cryosphere,* vol. 8, no. 5, pp. 1839-1854, 2014.

[60] T. Martin, *Arctic Sea Ice Dynamics: Drifts and Ridging in Numerical Models and Observations*. Alfred-Wegener-Institut für Polar-und Meeresforschung, 2007.

[61] P. J. Soille and M. M. Ansoult, "Automated basin delineation from digital elevation models using mathematical morphology," *Signal Processing,* vol. 20, no. 2, pp. 171-182, 1990.

[62] S. Mock, A. Hartwell, and W. Hibler III, "Spatial aspects of pressure ridge statistics," *Journal of Geophysical Research,* vol. 77, no. 30, pp. 5945-5953, 1972.

[63] W. Hibler III, W. Weeks, and S. Mock, "Statistical aspects of sea‐ice ridge distributions," *Journal of Geophysical Research,* vol. 77, no. 30, pp. 5954-5970, 1972.

[64] B. E. Schutz, H. J. Zwally, C. A. Shuman, D. Hancock, and J. P. DiMarzio, "Overview of the ICESat mission," *Geophysical research letters,* vol. 32, no. 21, 2005.

[65] M. Unser, A. Aldroubi, and M. Eden, "B-spline signal processing. I. Theory," *IEEE transactions on signal processing,* vol. 41, no. 2, pp. 821-833, 1993.

[66] M. L. McHugh, "The chi-square test of independence," *Biochemia medica,* vol. 23, no. 2, pp. 143-149, 2013.

[67] M. Webster *et al.*, "Snow in the changing sea-ice systems," *Nature Climate Change,* vol. 8, no. 11, pp. 946-953, 2018.

[68] A. Oikkonen, J. Haapala, M. Lensu, J. Karvonen, and P. Itkin, "Small‐scale sea ice deformation during N‐ICE 2015: From compact pack ice to marginal ice zone," *Journal of Geophysical Research: Oceans,* vol. 122, no. 6, pp. 5105-5120, 2017.

[69] R. Kwok, "Sea ice convergence along the Arctic coasts of Greenland and the Canadian Arctic Archipelago: Variability and extremes (1992–2014)," *Geophysical Research Letters,* vol. 42, no. 18, pp. 7598-7605, 2015.

[70] Y. Ye *et al.*, "Inter-comparison and evaluation of Arctic sea ice type products," *The Cryosphere,* vol. 17, no. 1, pp. 279-308, 2023.

[71] H. Stern and R. Lindsay, "Spatial scaling of Arctic sea ice deformation," *Journal of Geophysical Research: Oceans,* vol. 114, no. C10, 2009.

[72] N. Kimura and M. Wakatsuchi, "Increase and decrease of sea ice area in the Sea of Okhotsk: Ice production in coastal polynyas and dynamic thickening in convergence zones," *Journal of Geophysical Research: Oceans,* vol. 109, no. C9, 2004.

[73] P. Rampal, J. Weiss, and D. Marsan, "Positive trend in the mean speed and deformation rate of Arctic sea ice, 1979–2007," *Journal of Geophysical Research: Oceans,* vol. 114, no. C5, 2009.

[74] P. Itkin *et al.*, "Thin ice and storms: Sea ice deformation from buoy arrays deployed during N‐ICE 2015," *Journal of Geophysical Research: Oceans,* vol. 122, no. 6, pp. 4661-4674, 2017.

[75] L. Jakobson, T. Vihma, and E. Jakobson, "Relationships between sea ice concentration and wind speed over the Arctic Ocean during 1979–2015," *Journal of Climate,* vol. 32, no. 22, pp. 7783-7796, 2019.

[76] D. Clemens-Sewall, M. M. Smith, M. M. Holland, C. Polashenski, and D. Perovich, "Snow redistribution onto young sea ice: Observations and implications for climate models," *Elem Sci Anth,* vol. 10, no. 1, p. 00115, 2022.

[77] V. P. Walden, S. Murphy, S. R. Hudson, and L. Cohen, "N-ICE2015 atmospheric turbulent fluxes [Data set]," ed: Norwegian Polar Institute, 2017.

[78] C. J. Cox *et al.*, "Continuous observations of the surface energy budget and meteorology over the Arctic sea ice during MOSAiC," *Scientific Data,* vol. 10, no. 1, p. 519, 2023.

[79] A. K. DuVivier, M. M. Holland, S. J. Vavrus, L. Landrum, C. A. Shields, and R. Thaker, "Arctic sea ice loss drives increasing Arctic wind speeds with combined impact on surface roughness and boundary layer stability," 2022.

[80] J. Sterlin, M. Tsamados, T. Fichefet, F. Massonnet, and G. Barbic, "Effects of sea ice form drag on the polar oceans in the NEMO-LIM3 global ocean–sea ice model," *Ocean Modelling,* p. 102227, 2023.